

Mechanistic Insights into Oxygen Dynamics in Soot Combustion over Cryptomelane Catalysts in Tight and Loose Contact Modes via $^{18}\text{O}_2/^{16}\text{O}_2$ Isotopic Variable Composition Measurements – A Hot Ring Model of the Catalyst Operation

Joanna Gryboś,* Monika Fedyna, Piotr Legutko, Bartosz Leszczyński, Janusz Janas, Anna Wach, Jakub Szlachetko, Xuehua Yu, Andrzej Kotarba, Zhen Zhao, and Zbigniew Sojka*



Cite This: *ACS Catal.* 2021, 11, 9530–9546



Read Online

ACCESS |



Metrics & More



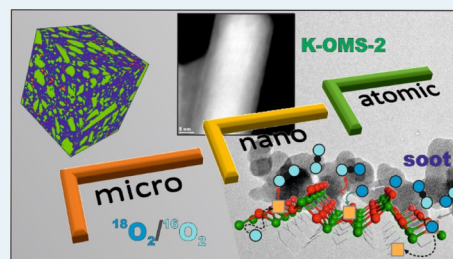
Article Recommendations



Supporting Information

ABSTRACT: A cryptomelane K-OMS-2 model catalyst of a well-defined nanorod morphology, dominated by the (100) and (110) planes, was synthesized, and thoroughly examined by means of XRD, Raman, XPS, XAS, TEM/EDX/SAED, and computed X-ray microtomography techniques. The catalyst oxidation performance was elucidated in the tight (TC) and loose (LC) contact modes using isotopic $^{18}\text{O}_2/^{16}\text{O}_2$ mixtures of various compositions. A simple methodology disentangling the relative involvement of the suprafacial (adsorbed/gas phase) and intrafacial (surface/lattice) reactive oxygen species in the soot oxidation was developed, allowing for straightforwardly unraveling the mechanistic details of the LC and TC combustion of soot particles. A functional “hot ring model” was established to rationalize the catalyst operation. It was found that apart from the ROS generation function, the catalyst acts in the TC mode as an igniter, whereas in the LC mode as a booster that drives the combustion process until the afterburning stage is reached. The obtained results were accounted for by molecular DFT and atomistic thermodynamic modeling, justifying the particular role of the surface di- (O_{2c}) and tri-coordinated (O_{3c}) oxygen anions, located on the (100) and (110) planes of the cryptomelane nanorods, in the ignition process.

KEYWORDS: K-OMS-2, DFT, first principles thermodynamics, oxidation, tomography, redox, mechanism



1. INTRODUCTION

Diesel engine devices and vehicles are one of the major sources of soot particle emission, contributing to proliferation of particulate matter (mainly $\text{PM} < 2.5 \mu\text{m}$), and polluting air in urban areas.^{1,2} Micrometric soot grains can be described as a mixture of crystalline and amorphous forms of carbon, which are intermingled with polycyclic and long-chain hydrocarbons.³ Constant strengthening of the diesel PM emission standards (EURO 6 or China 6) provides a steady incentive for development of effective technologies for soot emission abatement.^{4,5} The temperature of autogenic soot combustion (around 600 °C) is higher than that of the exhaust gases produced by diesel engines (200–400 °C). Thus, searching for low-cost catalytic materials that may successfully operate below 300–400 °C is currently one of the main challenges for development of efficient and durable catalytic particle filters (CDPF), which are based on earth-abundant components. Although owing to their superior activity, supported highly dispersed platinum group metals have dominated the automotive deSoot catalysis, their high cost and limited availability have triggered a continuous search for alternative cheaper materials.^{6,7} Among many examined transition metal oxide systems such as spinels and perovskites or ceria-based

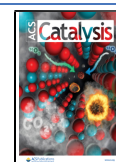
materials, often functionalized by addition of alkali (K, Na, Li, Rb, and Cs) or f-type metals (La and Pr),^{8–11} mixed oxide systems ($\text{Bi}_2\text{O}_3\text{--Fe}_2\text{O}_3$,¹² $\text{Cu/BaO/La}_2\text{O}_3$,¹³ CuO/SiO_2 , or $\text{Fe}_2\text{O}_3/\text{SiO}_2$ ^{14,15} along with manganese (Mn_2O_3)¹⁶ and potassium manganese oxides of layered (birnessite, OL)¹⁷ and tunnel (cryptomelane, OMS-2) structures^{18,19} exhibit promising performance as soot oxidation catalysts. Activity of the latter materials may further be improved upon doping with V, Nb, or Fe, which affects the physical and chemical properties of the cryptomelane matrix,^{20–22} the shape of crystallites, and the redox state of Mn, while maintaining the parent OMS-2 molecular architecture. Additional progress has been made by shape engineering of the catalysts, where 3DOM morphologies appear particularly beneficial.¹⁵

The cryptomelane ($\text{K}_x\text{M}_8\text{O}_{16}$) monoclinic structure ($I4/m$) is constituted by the edge-shared double 2×2 octahedral

Received: May 12, 2021

Revised: June 25, 2021

Published: July 16, 2021



MnO₆ chains, part of which are corner-shared forming one dimensional tunnels of 0.46 nm size. Different extra framework cations such as K⁺, Na⁺, H₃O⁺, Mg²⁺, or Ca²⁺ may be inserted into the tunnels, providing a compensating positive charge to increase stability of the OMS-2 structure. They also give rise to a mixed valence state of the manganese ions (coexistence of Mn⁴⁺, Mn³⁺, and Mn²⁺). As a result, the properties of OMS-2 materials can be tuned by replacement of the K ions in the tunnels, and by incorporation of iso- or alter-valent cations into the mixed-valent framework of the manganese octahedra.^{23,24} Such structural and redox versatility along with a clear cut morphology provide unique opportunities for exploring the structure–catalytic behavior relationships in soot oxidation at the molecular level. As a result, cryptomelane can be considered as a versatile prototype catalytic platform with expedient activity in soot combustion for model mechanistic investigations. Its sensible doping with alien cations allows for boosting its catalytic performance to a desired level for potential practical applications.

Although catalytic soot oxidation over various oxide catalysts has been widely studied,^{25,26} more detailed mechanistic investigations are rather scarce.²⁷ It is often tacitly assumed that the reaction turns over via the Mars van Krevelen mechanism,^{28–30} by involving extraction of a surface/lattice oxygen, O_{surf}^{2–}, with subsequent refilling of the resultant vacancies by gaseous O₂.³¹ However, it has been found that among a series of perovskites (LaCrO₃, LaFeO₃, and LaMnO₃), the K-substituted chromite catalyst (La_{0.9}K_{0.1}Cr_{0.9}O_{3–δ}) exhibits the highest deSoot activity, which is correlated with the amount of chemisorbed oxygen present on the surface.³² Reactive oxygen species (ROS) for soot combustion over LaMnO₃ were identified as O₂^{2–} and O₂[–] by operando Raman measurements,³³ and their role has been advanced in the case of, for example, Ag/CeO₂ catalysts.³⁴ Suprafacial ROS are also supposed to be involved in the NO to NO₂ oxidation, which is particularly beneficial for soot combustion in the loose contact (LC) mode.^{20,26}

There are several papers addressing those issues using isotopically labeled (O-18) dioxygen, though sometimes contradictory results have been reported. Most of the published results favor prime participation of O_{surf}^{2–} in the soot combustion reaction, even at low temperatures.^{35–37} In particular, the quantity of the surface oxygen involved in the isotopic exchange reaction has been associated with the activity of a Bi₂O₃–Co₃O₄ catalyst in soot oxidation.²⁹ Long-term isothermal isotopic experiments of soot combustion on yttria-stabilized zirconia, in turn, have shown that O^{2–} anions are operating at the soot/catalyst interface. The proposed account invokes an effective bismuth-induced surface oxygen exchange to replenish those O^{2–} anions that have been removed in the course of the soot oxidation.³⁸ In the case of much more intensively investigated ceria-based catalysts, it has been found that doping of CeO₂ with Pr and La enhances dioxygen exchange with the surface/lattice O^{2–} oxygen. A similar effect was observed in the case of Ag doping.³⁹ Therefore, the observed high soot oxidation activity even at low temperature could, again, be related to an increased contribution of such species in this reaction.³⁵ Based on sophisticated TAP studies of soot combustion over bare and Pt- or La-modified ceria, a more substantiated mechanism has been proposed, where soot oxidation was carried out by the O_{surf}^{2–} species, and not due to a direct reaction between O₂ and soot particles.⁴⁰ However, despite the progress made in this field, a systematic evaluation

of the role of various oxygen species in the soot combustion processes over oxide catalysts, including dynamic competition between the involvement of the adsorbed/gas phase oxygen (suprafacial mechanism) and the surface/lattice oxygen (intrafacial mechanism) at various stages of the reaction, is still not definitely resolved. Although both types of the redox mechanisms are widely recognized, their experimental verification is quite difficult, and often based on isotopically labeled reactants of single enrichment only. Reliable interpretation of such results is often not straightforward due to concurrent isotopic scrambling of the labeled gas-phase O₂ and CO₂ or with the catalyst surface and without any involvement of the redox step.⁴¹

In this paper, dynamics of the adsorbed (ROS) and surface oxygen (O_{surf}^{2–}) in the course of the soot oxidation over a model platform K-OMS-2 catalyst in the TC and LC modes was elucidated by means of comprehensive isotopic exchange studies using ¹⁸O-labeled oxygen, supported by TEM and X-ray tomography imaging of the catalyst-soot particles' spatial arrangements and interface contacts. The experimental results were supported by DFT and first principles thermodynamic modeling. The synthesized K-OMS-2 samples were thoroughly characterized by spectroscopic and microscopic techniques regarding their structure and morphology. Their catalytic activity in soot combustion was tested in the TC and LC using ¹⁶O₂, ¹⁸O₂, and ¹⁸O₂/¹⁶O₂ mixtures of regulated composition, and the Degussa-Printex U as a model soot. Evolution of the isotopically tagged reactants and products was used for the assessment of variable participation of the adsorbed and surface oxygen in different stages of the reaction in the loose and TC modes. According to our knowledge, mechanistic studies resolving the involvement of suprafacial (adsorbed/gas phase) and intrafacial (surface/lattice) oxygen, and providing direct insights into the TC and LC mechanisms of total soot combustion over K-OMS-2 and other oxide catalysts have not been carried out so far.

2. EXPERIMENTAL SECTION

2.1. Catalyst Synthesis. A cryptomelane (K-OMS-2) catalyst was synthesized according to the protocol described by Wasalathanthri et al.²¹ In a typical synthesis, 5.07 g of MnSO₄·H₂O was dissolved in solution of HNO₃ (1.8 mL) in the deionized water (18 mL). In the next step, 3.51 g KMnO₄ was dissolved in 60 mL of water, and then the obtained solution was transferred into a 300 mL round-bottom flask. The potassium permanganate solution was added dropwise to manganese sulfate solution under constant stirring and heating. The mixture was kept at about 100 °C under reflux with vigorous stirring for 24 h. The resulting material was filtered, washed using deionized water, dried in air at room temperature and then at 120 °C for 12 h, and finally calcined at 500 °C for 4 h. Commercial reagents such as MnSO₄·H₂O and KMnO₄ were provided by Sigma-Aldrich, while 65% HNO₃ was supplied by Avantor. A reference oxidized K-OMS-2-ox sample was obtained by oxidation of the parent K-OMS-2 in the flow of 50 mL/min of 100% O₂ at 550 °C for 2 h.

2.2. Catalyst Characterization. The crystalline structure of the synthesized cryptomelane was studied by means of X-ray diffraction using a Rigaku MiniFlex (PANalytical) instrument with nickel-filtered copper K α radiation (λ = 0.15406 nm). The scanning was carried out in the range of 2θ = 10–80° in the 0.02° steps at a counting time of 0.8 s per step. The crystallographic phase of the obtained K-OMS-2 was identified

by comparing the XRD pattern with the JCPDS database (reference 29-1020).

The morphology of the cryptomelane sample was examined with the use of a FEI Tecnai Osiris microscope operating at 200 kV, equipped with a X-FEG Schottky field emitter and a high-angle annular dark field (HAADF) detector (STEM mode). The information about the distribution of elements in the sample was obtained by the EDX analysis, using a windowless 4-sector silicon drift detector (Super-X EDX) and the Bruker ESPRIT software. Prior to TEM observations, the cryptomelane samples were placed on the copper grid covered with a holey carbon film.

The specific surface area (SSA, $\text{m}^2\cdot\text{g}^{-1}$) of the samples was measured by means of the five-point N_2 adsorption BET using a Quantasorb-1 analyzer. Prior to the measurements, the samples were outgassed at 180°C under a flow of helium for 4 h. The determined value of the specific surface area (BET) of the K-OMS-2 sample was equal to $57\text{ m}^2\cdot\text{g}^{-1}$.

Raman spectra were recorded at room temperature in the range of $100\text{--}3000\text{ cm}^{-1}$ with a Renishaw InVia spectrometer equipped with the Leica DM LM confocal microscope and a CCD detector. During Raman spectra recording, using the 788 nm excitation wavelength, nine scans were collected to ensure a satisfactory signal-to-noise ratio.

Computed X-ray microtomographic ($\mu\text{-CT}$) analysis of the samples was performed using a Bruker SkyScan 1172 micro-CT scanner with an energy of 80 keV and a pixel size of $1.38\text{ }\mu\text{m}$. The 2000×1332 pixel projection images were captured between the rotation steps of 0.4° . Each projection was averaged over 10 frames to increase the signal-to-noise ratio. For image reconstruction, the modified Feldkamp algorithm⁴² implemented in the GPU Nrecon software (v.1.7.3.2, Bruker micro-CT, Kontich, Belgium) was applied. Image processing and analysis was performed using the CT analyzer software (v.1.20.3.0, Bruker micro-CT, Kontich, Belgium). The samples were measured in a $10\text{ }\mu\text{L}$ pipet tip to get about a 1 mm diameter of the sample. The tip was mounted on a brass turntable with a hot glue to minimize sample movements during the scanning. The top of the pipet tip was covered with Parafilm M to prevent moisture absorption (Figure S1). For 3D analysis, a cubic volume of interest (VOI) with an edge of 0.7 mm was selected. The reconstructed image stacks were median filtered with a 3 pixel circular kernel, and for distinction of the boundaries, a histogram-based threshold was applied. The relative volume parameter describing the percentage of VOI occupied by the sample components and the catalyst particle size distribution were calculated.

2.3. Catalytic Activity Measurements. Thermo-programmed isotopic exchange experiments and the temperature-programmed oxidation of soot over the cryptomelane catalyst were performed in the temperature range of $50\text{--}750^\circ\text{C}$. All experiments were performed in a quartz fixed-bed reactor coupled with a QMS detector (Hidden Analytical HPR20) for CO ($\text{C}^{16}\text{O } m/z = 28$ and $\text{C}^{18}\text{O } m/z = 30$), CO_2 ($\text{C}^{16}\text{O}_2 m/z = 44$, $\text{C}^{16}\text{O}^{18}\text{O } m/z = 46$, and $\text{C}^{18}\text{O}_2 m/z = 48$), and O_2 ($^{16}\text{O}_2 m/z = 32$, $^{16}\text{O}^{18}\text{O } m/z = 34$, and $^{18}\text{O}_2 m/z = 36$) monitoring. The thermo-programmed isotopic exchange experiments were performed using 40 mg of cryptomelane. The soot combustion experiments were conducted using a model soot (Degussa–Printex U) mixed with the cryptomelane in a mass ratio of $1:10$. The samples were prepared by simple shaking for $\sim 10\text{ s}$ in an Eppendorf tube (loose contact, LC) and mixing in a mortar by grinding for $\sim 10\text{ min}$ (tight

contact, TC). All experiments were performed under a 2.5% O_2/He gas flow of $40\text{ mL}\cdot\text{min}^{-1}$, and at a heating rate of $10^\circ\text{C}\cdot\text{min}^{-1}$.

For the isotopic measurements, the $^{16}\text{O}_2/^{18}\text{O}_2$ mixtures of various ratios (98, 50, 30, 13, and 0% of $^{18}\text{O}_2$) were used. The molar fractions of the O_2 and CO_2 isotopomers were calculated from the raw QMS data using the following equations

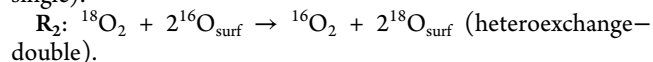
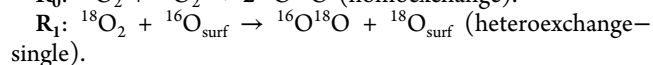
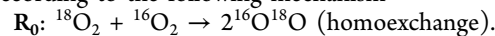
$$f_{ii} = I_{ii}/(I_{ii} + I_{jj} + I_{kk})$$

where $I_{ii} = 32$, $I_{jj} = 34$, and $I_{kk} = 36$ are the ion currents of dioxygen, whereas $I_{ii} = 44$, $I_{jj} = 46$, and $I_{kk} = 48$ are the ion currents of the carbon dioxide isotopomers. The atomic fractions of oxygen-16, α_{16} , in the gas-phase O_2 and CO_2 molecules were calculated from the corresponding molar compositions as

$$\alpha_{16}(\text{O}_2) = f_{34}/2 + f_{32}$$

$$\alpha_{16}(\text{CO}_2) = f_{46}/2 + f_{44}$$

The isotopic oxygen exchange with the catalyst may occur according to the following mechanism⁴³



2.4. Molecular Modeling. Periodical DFT + U modeling was performed with the VASP code using a projector augmented plane wave method (PAW), the PBE exchange-functional,⁴⁴ and the Hubbard parameter $U = 2.5\text{ eV}$. The Monkhorst–Pack grid⁴⁵ with a $3 \times 3 \times 5$ sampling mesh for bulk calculations and $3 \times 3 \times 1$ for slab calculations with a cutoff energy of 400 eV were applied. The bulk K-OMS-2 unit cell containing 26 ions ($\text{KMn}_8\text{O}_{16}$), and a (2×2) slab model exposing the (100) and (110) planes were used. A slab of $\sim 16\text{ }\text{\AA}$ thickness contains 13 atomic layers with the supercell $\text{KMn}_8\text{O}_{16}$ composition, whereas the vacuum separation was set to $15\text{ }\text{\AA}$. The atoms located in the top layers were relaxed, while applying a convergence value of $1 \cdot 10^{-3}\text{ eV}\cdot\text{\AA}^{-1}$.

To examine the defect structure and redox state of the exposed cryptomelane surfaces (110) and (100) under various T , p_{O_2} conditions, the ab initio thermodynamic modeling was applied.^{46,47} Within this approach, the free energy, γ , of the surface containing N_{O} oxygen atoms and N_{Mn} manganese atoms relative to the bulk $\text{KMn}_8\text{O}_{16}$ can be calculated as

$$\begin{aligned} \gamma(T, p_{\text{O}_2}) = & \frac{1}{2A} [G_{\text{KMn}_8\text{O}_y}^{\text{slab}}(T, p_{\text{O}_2}, N_{\text{Mn}}, N_{\text{O}}) \\ & - N_{\text{Mn}} G_{\text{KMn}_8\text{O}_{16}}^{\text{bulk}}(T, p_{\text{O}_2}) \\ & - (N_{\text{O}} - 2N_{\text{Mn}}) \mu_{\text{O}}(T, p_{\text{O}_2})] \end{aligned}$$

In the above equation, $G_{\text{KMn}_8\text{O}_y}^{\text{slab}}$ and $G_{\text{KMn}_8\text{O}_{16}}^{\text{bulk}}$ correspond to the free energy of the slab and the bulk, respectively, normalized to a formula unit ($\text{KMn}_8\text{O}_{16}$). Noting that the entropic vibrational contributions to the Gibbs free energies cancel to a large extent, their values were approximated by the corresponding DFT energies. The symbol A stands for the (1×1) surface area exposed by the slab, whereas $\mu_{\text{O}}(T, p_{\text{O}_2})$ is the chemical potential of dioxygen, factored into the electronic energy $(1/2E_{\text{O}_2}^{\text{tot}})$, the temper-

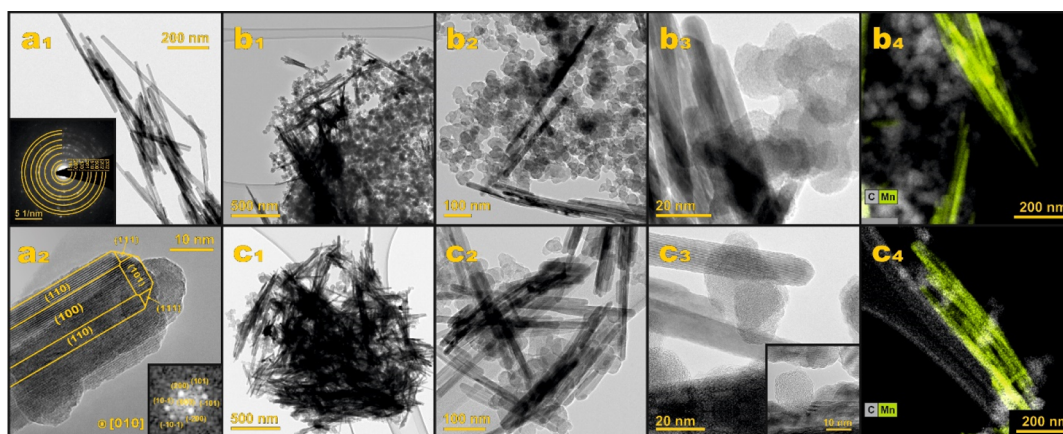


Figure 1. TEM/EDX/SAED analysis of the cryptomelane (K-OMS-2) nanorods (a₁,a₂), and their mixtures with soot nanoparticles in LC and TC contact modes, b₁–b₄, and c₁–c₄, respectively.

ature ($\mu_{\text{O}}'(T, p_{\text{O}_2}^0)$), and the pressure [$kT \ln(p_{\text{O}_2}/p^0)$]-dependent contributions

$$\mu_{\text{O}}(T, p_{\text{O}_2}) = \frac{1}{2}E_{\text{O}_2}^{\text{tot}} + \mu_{\text{O}}'(T, p_{\text{O}_2}^0) + kT \ln\left(\frac{p_{\text{O}_2}}{p^0}\right)$$

The electronic energy term, $1/2E_{\text{O}_2}^{\text{tot}}$, was calculated by DFT, whereas the $\mu_{\text{O}}'(T, p_{\text{O}_2}^0)$ term was computed by means of standard statistical thermodynamics.⁴⁸

3. RESULTS AND DISCUSSION

3.1. Morphological and Structural Characterization of the Catalyst. Phase purity of the synthesized cryptomelane (K-OMS-2) was examined by XRD (Figure S2a1) and Raman (Figure S2a2) techniques. The observed XRD reflections are fully consistent with the ICSD-59159 reference pattern of cryptomelane.⁴⁹ Among the $6A_g + 6B_g + 3E_g$ Raman active modes, seven bands can be distinguished in the registered spectra (Figure S2a2). The two intense A_g peaks at 630 and 574 cm^{-1} correspond to Mn–O stretching vibrations in the edge-sharing MnO_6 octahedra.⁵⁰ The band at 630 cm^{-1} is assigned to Mn–O vibrations that are perpendicular to the MnO_6 double chains,⁵⁰ whereas the band at 574 cm^{-1} is due to displacements of the oxygen anions with respect to the Mn cations along the octahedral chains. The narrow peak situated at 180 cm^{-1} is attributed to vibrations resulting from the hindered translational motion of the MnO_6 octahedra, and the weaker bands at 386 and 758 cm^{-1} correspond to O–Mn–O bending and antisymmetric Mn–O stretching vibrations, respectively.⁵⁰

The morphology of the K-OMS-2 nanocrystals and their elemental composition (K, Mn, and O mapping) are presented in Figure 1. The bright field TEM imaging (Figure 1a₁) reveals a distinct nanorod shape of the crystallites, extending preferentially along the [001] direction with the (100) and (110) planes being the most abundant. The average length of the nanorods is around 350 nm, and the corresponding average aspect ratio $\langle \text{AR} \rangle \sim 20$. The cryptomelane nanorods are randomly arranged into irregular bunches. As it can be deduced from the corresponding SAED patterns (Figure 1a₁,a₂), the K-OMS-2 nanorods preserve well their cryptomelane phase integrity and high crystallinity along their entire length. Moreover, they exhibit sharp edges with quite well-developed faceting at the (101) and (111) planes. A mapping

of the elemental composition of the K-OMS-2 nanorods was performed by the STEM/EDX techniques. The results show that the O/Mn = 0.63 and K/Mn = 0.12 ratios along and across the nanorods are quite uniform, implying that within the resolution of the EDX probe there is no significant variation in the spatial composition of the synthesized sample. The observed deviation from the nominal stoichiometry indicates that the resultant composition of the manganese dioxide backbone of the cryptomelane nanorods can be formulated as $\text{Mn}_{1-2x-y}^{4+}\text{Mn}_{2x}^{3+}\text{Mn}_y^{2+}\text{O}_{2-2x-y}$, as discussed previously by us in more detail.⁵¹

The imaging results of the nanometric scale agglomeration and intermingling between the cryptomelane nanorods and the soot nanoparticles are presented in Figure 1b₁–b₄, c₁–c₄, for the loose and TC modes, respectively. Due to their elongated morphology, the K-OMS-2 nanorods exhibit a clear tendency for agglomeration into rounded bundles (Figure 1b₁,c₁). In the case of the LC, the cryptomelane nanorods are surrounded by slackly agglomerated carbon particles with sparse direct contact points and profuse void spaces (1b₁, b₂). In the TC mixing, the soot particles and the nanorods are much better blended to produce compact assemblies, giving rise to the formation of abundant catalyst surface-soot contacts (Figure 1c₁,c₂). As can be inferred from the inset of Figure 2c₃, in the TC mode, the soot nanoparticles that are in a direct contact with the catalyst may significantly deform the surface of the cryptomelane nanorods, implying strong mutual interaction, imposed probably by the mechanochemical effects appearing in the course of grinding. For alternative illustration of the agglomeration and spatial distribution of the catalyst and the soot particles, EDX mapping was also performed (Figure 1b₄,c₄). The cryptomelane nanorods are represented therein by the Mn spatial distribution (marked in green), whereas the soot particles are shown in gray.

3.2. Spatial Arrangement of Soot and Catalyst Particles in the Tight Contact and Loose Contact. Mutual arrangements of the soot and catalyst particles in the TC and LC modes on the micrometric scale, revealed by means of the X-ray microtomography, are shown in Figure 2.

In the case of the TC mode, Figure 2a₁ shows that within the submillimetric VOI, the interlaced cryptomelane nanoneedles, observed in TEM pictures, are further agglomerated into larger micrometric grains of a pronounced size dispersion. This can be inferred from the corresponding color-coded

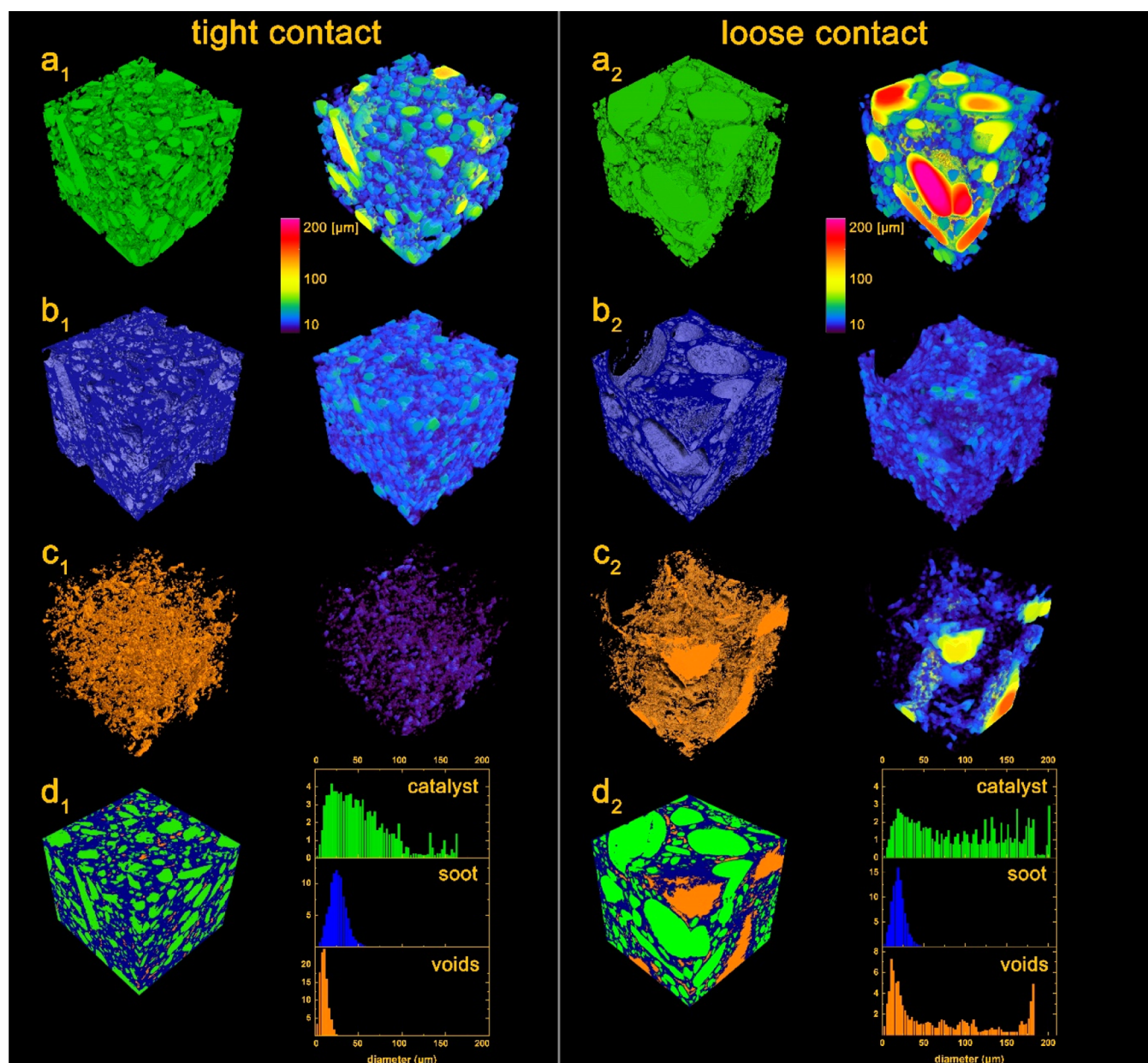


Figure 2. μ -CT images of the K-OMS-2 mixture with soot particles in tight (a_1 – d_1) and loose (a_2 – d_2) contact modes, along with the corresponding size distribution histograms of the catalyst grains, soot particles, and empty voids. Spatial distribution of the catalyst grains (a_1 and a_2), soot particles (b_1 and b_2), and empty voids (c_1, c_2), and the compact catalyst-soot assemblies (d_1 and d_2) are shown using the corresponding color rendering. Due to the micrometric resolution of the technique, the nanometric features (nanorod structure observed in TEM) are smeared out.

volume-rendered model shown in the right image. The catalyst grains are surrounded by the tightly packed soot particles (Figure 2 b_1 , right and left), leaving, however, small empty voids (Figure 2 c_1 right and left), randomly distributed throughout the analyzed VOI in a rather homogeneous fashion. Those soot particles that are not in a direct contact with the catalyst are quite densely packed. The resultant compact catalyst-soot assembly is shown in Figure 2 d_1 , with the corresponding size distribution histograms of the catalyst grains, soot particles, and empty voids (right panel). A quick inspection of the histograms reveals a small size of the voids (centered around 12 μm) produced upon TC mixing and their narrow distribution (Figure 2 d_1). The soot particles exhibit an average size of 25 μm , which implies that similar to the catalyst

grains, soot nanoparticles of the 10–20 nm parent size are also agglomerated into larger forms containing several dozens of the pieces, as revealed in the TEM images as well (vide infra). In contrast to the soot agglomerates, the catalyst grains show a much larger size and broader distribution, tailing till $\sim 160 \mu\text{m}$. Due to the micrometric resolution of the μ -CT technique, the nanometric features of the cryptomelane nanorod structure observed in TEM (Figure 1 a_1, a_2) are smeared out in the catalyst μ -CT images. In conclusion, the TC mode leads to the formation of a compact catalyst-soot structure with only a minor contribution of the empty voids, which are well dispersed within the examined VOI.

In the LC mode, the catalyst grains are substantially more heterogeneous in size with the presence of few significantly

large pieces (Figure 2a₂ left and right). Despite the overall packing of the soot particles is similar to that observed in the TC (Figure 2b₂ left and right), large cavities (100–200 μm) tinned in yellow/orange are present simultaneously with abundant empty spaces smaller in size, which are tinned in purple/blue (Figure 2c₂ left and right). As a result, in the pronounced contrast to the TC packing, a substantial fraction of the examined volume remains empty in the LC mode (Figure 2d₂). Furthermore, the 3D structure separation parameter, defined as a maximal sphere diameter that can fit between the grains, was also determined. The LC sample, on average, exhibits more than twice the separation between the sample structures (soot vs catalyst grains) in comparison to the TC.

3.3. Surface Oxygen Dynamics and Availability. Prior to soot oxidation tests, the K-OMS-2 catalyst was examined in the context of adsorbed (ROS) and surface ($\text{O}_{\text{surf}}^{2-}$) oxygen dynamics, and their specific availability in oxidation processes, in a series of temperature-programmed experiments. Release of the surface oxygen was evaluated at low ($p_{\text{O}_2} \sim 10^{-6}$ mbar, simulated by pure He flow) and medium ($p_{\text{O}_2} \sim 10^{-2}$ (2.5 mol % O_2/He flow) oxygen pressures, and the results are shown in Figure 3a,b. In the former case, the oxygen evolution exhibits

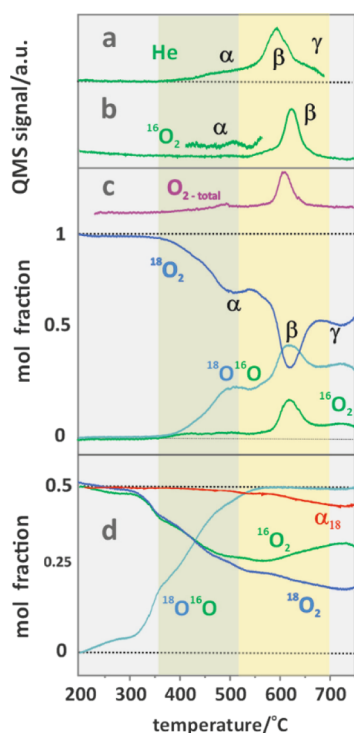


Figure 3. Temperature-programmed oxygen release in the flow of He (a), $^{16}\text{O}_2$ (b), and $^{18}\text{O}_2$ exchange with the surface (c), and isotopic $^{18}\text{O}_2/^{16}\text{O}_2$ equilibration over the surface of K-MSO-2 (d). The shaded areas correspond to the temperature windows of the TC (pale gray–greenish) and LC (pale yellow) soot combustion.

two distinct desorption peaks, a weaker and broad one labeled α , appearing in the temperature range 350–550 $^{\circ}\text{C}$, and a stronger peak β centered around ~ 590 $^{\circ}\text{C}$. The latter is followed by a shoulder γ that extends into the higher temperatures (Figure 3a). The change in the stoichiometry associated with the dominant β peak at ~ 590 $^{\circ}\text{C}$ corresponds to $\sim 13\%$.

In an analogous measurement performed in the flow of $^{16}\text{O}_2$, the α peak is apparently less manifested (due to the buffering effect of the flowing $^{16}\text{O}_2$), whereas the central β peak is shifted by ~ 50 $^{\circ}\text{C}$ toward higher temperatures. We associate the broad α peak with adsorbed reactive oxygen species ($\text{O}_{\text{n-ads}}^{-}$) and with low coordinated surface oxygen $\text{O}_{\text{surf}}^{2-}$ (explicitly $\text{O}_{2\text{c}}^{2-}$) release (the subscript indicates here the coordination number). The most pronounced β peak, in turn, corresponds to an intensive discharge of the surface $\text{O}_{2\text{c}}^{2-}$ and $\text{O}_{3\text{c}}^{2-}$ species resulting in the formation of multiple vacancies (see below). A more detailed insight into the dynamics of the surface oxygen was obtained by means of temperature-programmed isotopic exchange (TPIE) of the gaseous $^{18}\text{O}_2$ with the suprafacial ($^{18}\text{O}_{2(\text{g})}/^{16}\text{O}_{\text{n-ads}}^{-}$ exchange) and the intrafacial ($^{18}\text{O}_{2(\text{g})}/^{16}\text{O}_{\text{surf}}^{2-}$ exchange) oxygen species.

The results shown in Figure 3c reveal that the isotopic exchange (scrambling) of gaseous $^{18}\text{O}_2$ with the K-OMS-2 surface begins above 340–350 $^{\circ}\text{C}$, reaching a plateau in the range of 500–550 $^{\circ}\text{C}$. Then, it further increases evolving into an apparent band with the maximum at ~ 620 $^{\circ}\text{C}$, and a weaker one above 700 $^{\circ}\text{C}$. The positions of these maxima may be traced back to the α , β , and γ peaks observed in Figure 3a,b. The relative content of the $^{16}\text{O}^{18}\text{O}$ isotopomer is much higher than that of $^{16}\text{O}^{16}\text{O}$ in the whole temperature range, indicating that the R_1 (single exchange) mechanism dominates over the R_2 (double exchange) one. The latter is practically insignificant below 550 $^{\circ}\text{C}$, but next is obscured by release of surface oxygen-16 with the maximum around 630 $^{\circ}\text{C}$. It is worth noting that during this experiment, the total oxygen pressure until the temperatures before the β -peak increases just slightly, implying a small surface reduction of the catalyst only. The observed minor reduction of the catalyst indicates that, once the temperature increases (or oxygen pressure decreases) as the reaction progresses, the catalyst changes its redox state by generation of the oxygen vacancies to maintain an equilibrium with the actual chemical potential of the gas phase oxygen (catalyst redox autotuning). This behavior has been observed previously in the case of CH_4 oxidation over a cobalt spinel catalyst.⁵² Such a slender reduction of the surface is then beneficial for activation of dioxygen, compensating its temporary dropping pressure as the soot conversion accelerates (vide infra). As a result, in the temperature range of soot combustion in the TC mode (marked by a pale gray–greenish stripe), the K-OMS-2 catalyst is redox-tuned yet virtually redox stable. While in the LC mode (yellowish stripe), the temperature window of the catalyst operation overlaps with the β peak region of the surface oxygen release, where the maximum in the isotopic exchange and appreciable local reduction occurs ($\sim 13\%$). Indeed, in the corresponding XRD and RS spectra, new features attributed to manganese oxides in the lower oxidation state (Mn_2O_3 – Mn_3O_4) can be distinguished (Figure S2c1,c2). However, upon passing the β peak, the altered catalyst becomes redox stable again.

In the next step of the surface characterization, equilibration of the equimolar $^{18}\text{O}_2/^{16}\text{O}_2$ mixture was used to probe the dissociative activation of dioxygen over the K-OMS-2 catalyst (Figure 3d). The extent of maintenance of the suprafacial character of this reaction was monitored by calculation of the α_{18} parameter (red line). The isotopic exchange reaction occurs quite readily starting already at ~ 200 $^{\circ}\text{C}$, and just above 500 $^{\circ}\text{C}$, it is practically accomplished. In this temperature range, the suprafacial character of the isotopic exchange dominates, as revealed by the nearly constant α_{18} value. Upon

crossing a temperature threshold of 500 °C, a gradual enhancement of the scrambling with the surface $^{16}\text{O}_{\text{surf}}^{2-}$ anions gains importance. It is reflected in the progressive divergence of the $^{18}\text{O}_2$ and $^{16}\text{O}_2$ profiles with the increasing temperature, and in a concise way, by the steady dropping of the α_{18} value as well (Figure 3d). Evolution of the $^{16}\text{O}^{18}\text{O}$ profile shows some irregularities (turning points), implying that different centers may participate in dioxygen activation, with their particular involvements varying as the temperature increases. In conclusion, the results described above provide a useful reference background for mechanistic interpretation of the soot oxidation reaction over the K-OMS-2 catalyst under model conditions (i.e., without NO), which is discussed below.

3.4. Redox Behavior of the Catalyst. For straightforward operation of the redox mechanism of soot combustion over the cryptomelane catalyst, the reduction and oxidation steps have to occur efficiently and in a congruent way during the reaction course. Yet, the progress of those steps cannot be measured individually under the real reaction conditions. Thus, the efficiency of the K-OMS-2 reduction (oxygen release) and subsequent reoxidation (oxygen storage) was probed by isothermal alternating pulses of CO and O_2 over the catalyst surface, performed at selected temperatures below the threshold of the spontaneous oxygen release (600 °C). Typical gas concentration profiles recorded at the inlet and outlet of the reactor when equimolar CO and O_2 pulses are alternatively switched at various temperatures are shown in Figure 4. In all

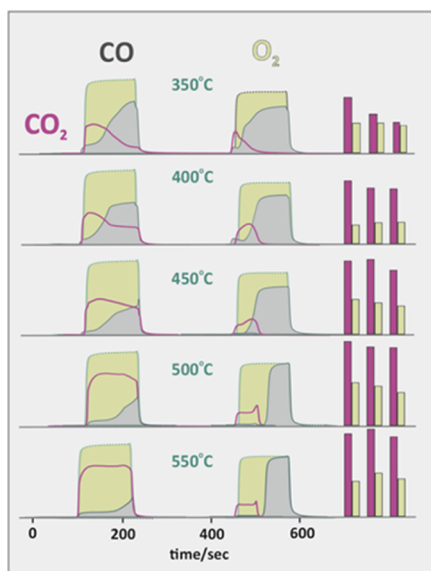


Figure 4. Isothermal gas concentration profiles of CO_2 , CO, and O_2 upon sequential pulsing of CO and O_2 on the K-OMS-2 catalyst at various temperatures (left), together with the corresponding integrated surface areas of the reduction and oxidation peaks (right). Purple line— CO_2 profile, pale green-shaded region—inlet peak, and gray-shaded region—outlet peak.

the performed redox cycles, the K-OMS-2 catalyst surface was first reduced and next reoxidized. Analysis of the CO uptake process shows a two stage CO oxidation, with the early stage being much faster than the late one. This finding suggests involvement of two types of lattice oxygen of distinct activity, which is consistent with the presence of the α and β peaks in Figure 3b. However, regardless of the temperature of the reaction, a part of the injected CO is not completely oxidized

by the surface oxygen ($\text{O}_{\text{surf}}^{2-}$). The residual adsorbed CO remains on the catalyst surface during helium purge until it becomes readily oxidized by the first amounts of dioxygen introduced in the subsequent pulse, giving rise to the corresponding weaker CO_2 echo. A similar behavior was observed previously in the case of CO/ O_2 cycling over $\text{CeO}_2/\text{La}_2\text{O}_2\text{SO}_4$ catalysts.⁵³

The cumulative amount of CO_2 produced (equal to CO consumed) under the anoxic conditions is equivalent to the corresponding O_2 uptake. The concentration profiles of the O_2 peaks (upon initial oxidation of the residual CO) show strong uptake that increases with the growing temperature. Their distinctly regular shapes, most apparent at low temperatures, suggest that the catalyst reoxidation does not occur as a single process. The relative amounts of the CO_2 production and O_2 consumption in the three consecutive pulses, calculated from the integral area of the CO_2 peaks (purple bars) and the difference between the areas of the inlet ($\text{O}_{2\text{in}}$) and the outlet ($\text{O}_{2\text{out}}$) pulses (pale green bars), may be treated as a measure of the congruence of the catalyst reduction and reoxidation steps. At 350 °C, the average ratio $\langle(\text{O}_{2\text{in}} - \text{O}_{2\text{out}})/\text{CO}_2\rangle$, which is equivalent to $\langle\text{O}_2(\text{consumed})\rangle/\langle\text{CO}(\text{consumed})\rangle$, was equal to 0.66 indicating that the catalyst at lower temperatures is resultantly oxidized, and then it drops to 0.41. In the temperature range of 450–550 °C, however, the $\langle(\text{O}_{2\text{in}} - \text{O}_{2\text{out}})/\text{CO}_2\rangle$ values approach a nearly stoichiometric level of 0.47–0.49. These results reveal that the redox properties of the K-OMS-2 catalyst in the temperature window of soot oxidation interest are fairly well equilibrated, when the momentary deviations from the stoichiometry, controlled by the size of the CO/ O_2 pulses, are reasonably small. The stoichiometric reduction and oxidation may be then stably cycled in the temperature range of the soot oxidation interest. It is worth emphasizing that during the soot combustion process, the catalyst surface may transiently be much more deeply reduced. Especially, around the combustion peak maximum in the TC mode, due to local overheating caused by high exothermicity of the soot oxidation process. Nonetheless, once the soot combustion is fully accomplished, in the presence of oxygen, the redox state of the catalyst surface may be effectively regenerated below 600 °C.

In order to evaluate the redox behavior of K-OMS-2 in a larger temperature range (100–700 °C), we performed XAS measurements of this catalyst in the flow of 5% O_2/He .

The XAS spectra recorded in situ at the beginning (100 °C) and the end (700 °C) of the thermal treatment under the flow of 5% oxygen are shown in Figure 5a, together with the reference spectra of Mn_3O_4 and MnO_2 . The corresponding changes in the average oxidation state of Mn cations (Figure 5b) are rather small, varying from AOS = 3.67–3.68 at the beginning to 3.5–3.6 upon reaching 700 °C. Analysis of the continuous alternation of the AOS values with the temperature (Figure 5c) reveals that the KOMS-2 catalyst is just slightly reduced with the increasing temperature, due to a steady loss of the weakly bound $\text{O}_{2c}/\text{O}_{3c}$ (100) and O_{2c} (110) surface oxygen species (see below). Although the catalyst surface becomes defected because of the oxygen vacancy formation, generally, the K-OMS-2 catalyst seems to be reasonably stable in the temperature window of the soot oxidation reaction, maintaining the Mn average oxidation state in the range of 3.57–3.7 in the presence of dioxygen in the gas mixture.

3.5. Catalytic Tests. In order to understand how the contact points between the catalyst and soot particles influence

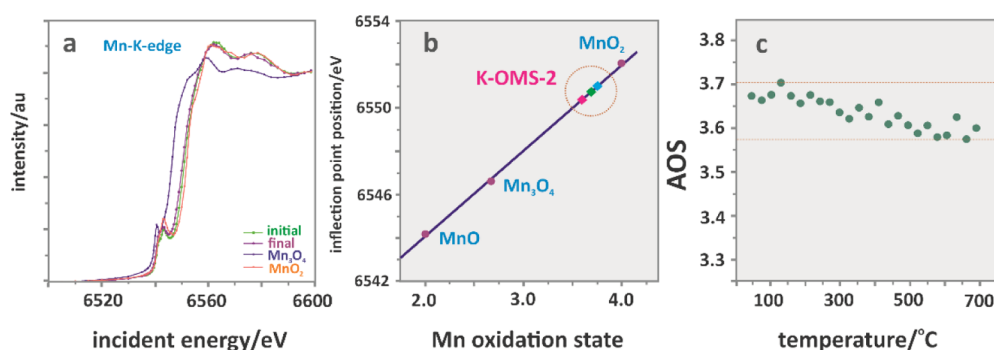


Figure 5. XAS spectra of the K-OMS-2 catalyst recorded in the flow of 5% of oxygen at the beginning (100 °C) and at the end (700 °C) of thermal treatment, along with the reference spectra (a), determination of average oxidation state of manganese (b), and temperature variation of the Mn redox state (c).

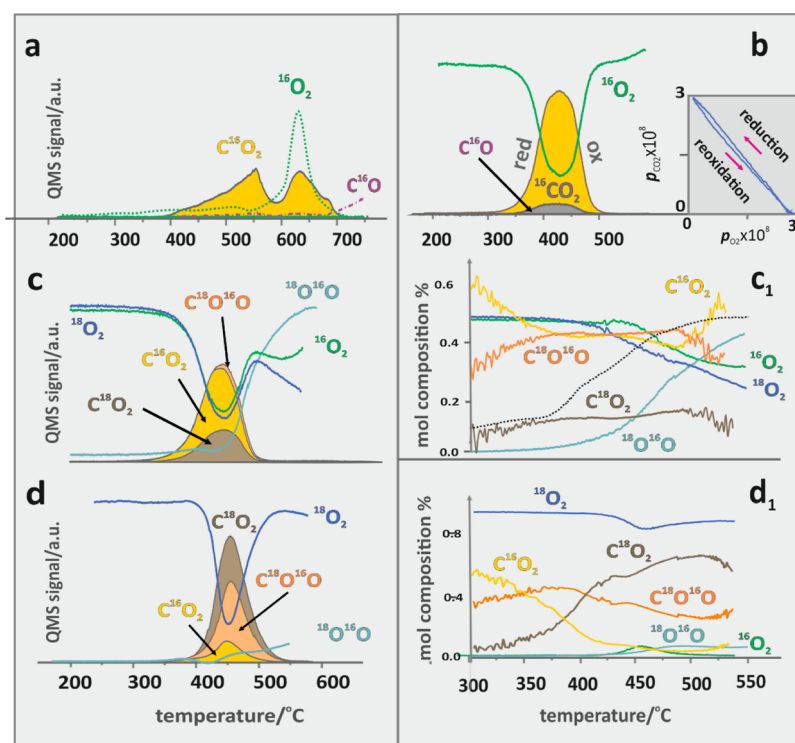


Figure 6. QMS profiles of dioxygen and CO₂/CO recorded during soot combustion over the K-OMS-2 catalyst in the TC mode under anoxic conditions (a), in the flow of ¹⁶O₂ (b), in a ¹⁶O₂ and ¹⁸O₂ 1:1 mixture (c), and in ¹⁸O₂ (d). The corresponding molar compositions of the products (calculated separately for the O₂ and CO₂ isotopomers) are shown in c₁ and d₁, respectively. The inset in (b) shows the parity plot of the changes in the normalized $p(\text{O}_2)$ vs $p(\text{CO}_2)$ during the combustion reaction.

the course of the combustion process and the redox stability of the catalyst, isotopic experiments were performed using ¹⁸O₂/¹⁶O₂ mixtures of various isotopic composition (VIC) in the TC and LC modes. Prior to the relevant catalytic tests, reference experiments of a noncatalytic soot combustion in ¹⁸O₂, and isotopic scrambling of ¹⁸O₂ with CO₂ were additionally performed. As shown in Figure S3a, the bare soot combustion onset appears around 500 °C. However, Figure S3b shows that already above 350 °C an appreciable release of C¹⁶O₂/C¹⁶O due to surface decarboxylation and decarbonylation takes place, which is accompanied by a trace oxidation of the soot particles (latent combustion). As a result, below ~400 °C, where the combustion process remains still in its incipient state, the reaction products are featured by an enhanced contribution of C¹⁶O and C¹⁶O₂, which decay tails even till 650 °C. Noticeably, the remnants of C¹⁶O¹⁸O are even

observed in the whole temperature range. Within the temperature window of proper combustion (500–800 °C), the reaction products are dominated by C¹⁸O, which evolves in a noticeably different way than C¹⁸O₂, implying that both products are produced along separate reaction pathways (e.g., by thermal decomposition of adjacent carboxylic groups and surface decarbonylation), as revealed by our previous TOF–SIMS studies corroborated by DFT modeling.⁵⁴

Scrambling of the labeled reactants and products leads to undesired masking of the results of the isotopic soot combustion experiments, which can make interpretation of the obtained results rather challenging. To support the analysis of the labeled soot combustion products, we examined a temperature-programmed isotopic exchange between C¹⁶O₂ and ¹⁸O₂, and the corresponding TPIE profiles (variation of the molar composition of all involved isotopomers with

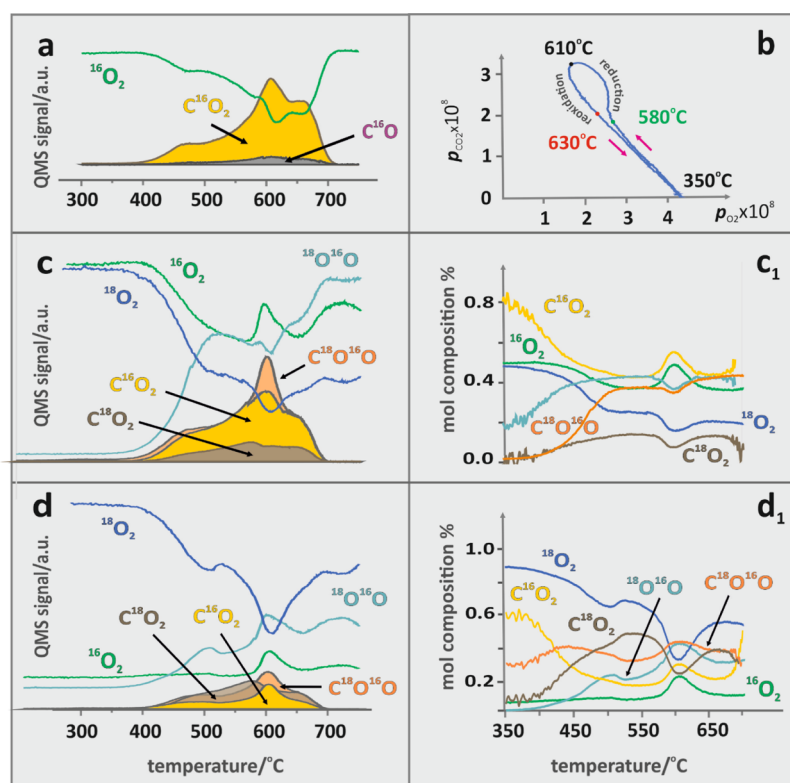


Figure 7. QMS profiles of dioxygen and CO₂/CO recorded during the soot combustion over the K-OMS-2 catalyst in the LC mode in the flow of ¹⁶O₂ (a), in the ¹⁶O₂ and ¹⁸O₂ 1:1 mixture (c), and in ¹⁸O₂ (d). The corresponding molar compositions of the products (calculated separately for the O₂ and CO₂ isotopomers) are shown in c₁ and d₁, respectively. The parity plot of the changes in the normalized $p(\text{O}_2)$ vs $p(\text{CO}_2)$ pressures during the combustion reaction is shown in (b).

temperature) are shown in Figure S3c. As indicated by the emergence of C¹⁶O¹⁸O, the isotopic scrambling begins at 350 °C, and around 500 °C an equilibrium composition of the gas mixture is reached. Until ~600 °C, the scrambling process takes place predominantly with an involvement of the suprafacial O-18 species, which is implied by the shape of the $\alpha_{18}(\text{O}_2)$, $\alpha_{18}(\text{CO}_2)$, and $\alpha_{18}(\text{total})$ profiles. The catalyst surface O_{surf}²⁻ species are thus apparently quite inert in this process. However, in the temperature window ~600–670 °C, the observed drop of all the α_{18} values indicates that an enhanced exchange of ¹⁸O₂ with the K-OMS-2 catalyst takes place in this temperature region, due to spontaneous liberation of the surface oxygen species (vide infra). Above the temperature threshold of this transformation, the catalyst surface becomes stable again, as in the case of the oxygen release observed in the corresponding isotopic exchange studies (Figure 3).

3.5.1. Tight Contact Combustion. The results of the catalytic screening of soot combustion in the TC mode performed with different experimental protocols are shown in Figure 6. At the beginning, an anoxic combustion of soot was used to probe the inherent activity of the surface oxygen (O_{surf}²⁻) of the K-OMS-2 catalyst. The reaction occurs in a trimodal way over a broad temperature range, starting from ~350 to 750 °C, as it can be inferred from the CO₂ and CO profiles shown in Figure 6a.

The first CO₂ band (with the maximum at 580 °C) is associated with oxidation of soot particles that are in direct contact with the catalyst surface. Gradual depletion of such contacts during the progressing reaction leads to an apparent drop in the combustion efficiency, yet owing to subsequent

release of the surface oxygen with the increasing temperature (see the green-dotted line), the combustion efficiency is regained as manifested by the maximum at 640 °C. The appearance of the dominant CO at the highest temperatures only is indicative of the burn-off of the remote soot particles (visible in Figure 1c₁) by the liberated dioxygen molecules because excessive CO is a diagnostic product of the bare soot combustion in O₂ (see in Figure 6a).

In the presence of dioxygen, the dynamics of the combustion process is changed dramatically. It is shifted to lower temperatures (320–500 °C), and occurs in a thermally abrupt fashion (Figure 6b). Indeed, the high exothermicity of soot combustion gives rise to a high local temperature increase, enabling straightforward accomplishment of the combustion process within a single exotherm only, and with a superior CO₂ selectivity as well. A more detailed analysis of the parity plot, for the mutual variation of the normalized $p\text{O}_2$ vs $p\text{CO}_2$, shows that before reaching the combustion maximum at $T = 420$ – 430 °C, the catalyst is slightly reduced as $p\text{CO}_2 > p\text{O}_2$. However, then it is gradually reoxidized when the combustion process is ceasing due to the soot depletion (see the CO₂ and O₂ profiles in Figure 6b and the corresponding hysteresis in the inset). Upon passing the combustion peak, the hysteresis disappears showing that the catalysts resume their redox steady state.

A much more detailed insight into the intimate course of the TC soot combustion was obtained from the isotopic experiments. The results for the oxidation reaction in an equimolar mixture of ¹⁶O₂ and ¹⁸O₂ and in ¹⁸O₂ alone are shown in Figure 6c₁, d₁, respectively. In the case of soot combustion in a 1:1 mixture of ¹⁶O₂/¹⁸O₂, the main products

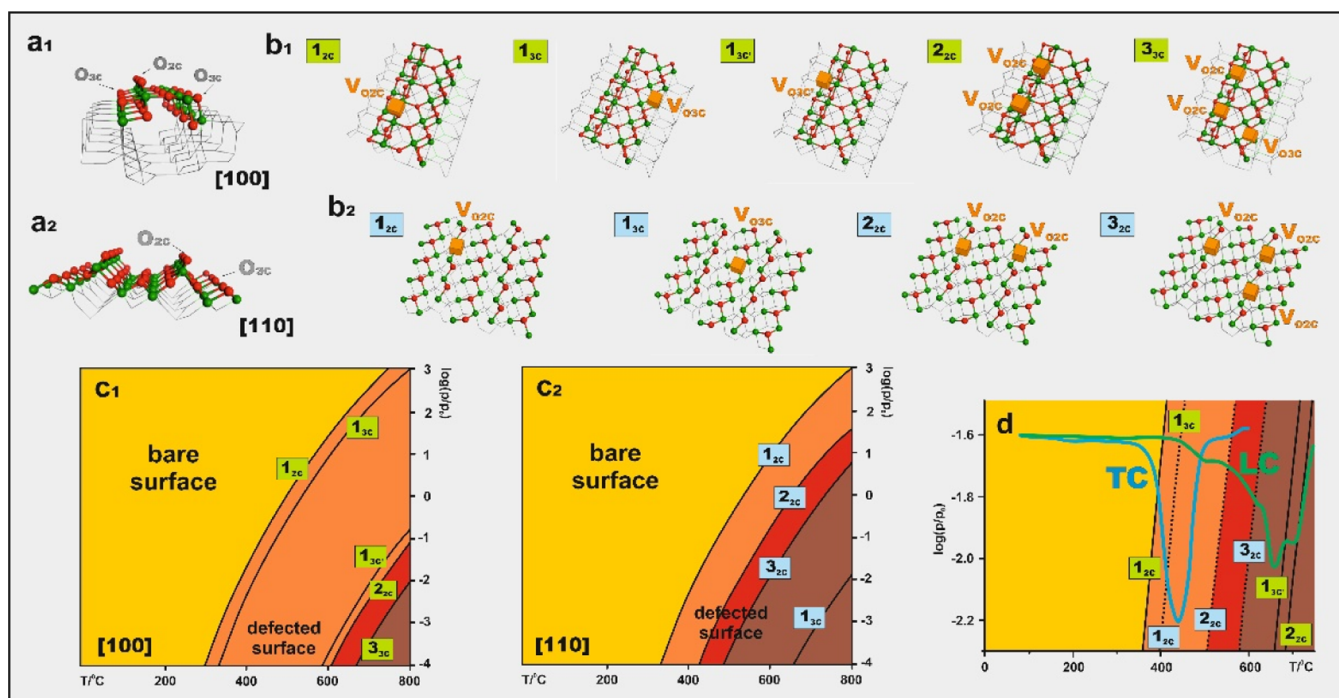


Figure 8. Optimized geometry of the stoichiometric most abundant (100) and (110) planes of the K-OMS-2 catalyst (a₁, a₂), and the corresponding oxygen vacancies with the positions marked by the orange boxes (b₁, b₂). Thermodynamic stability regions of the bare (adsorption of oxygen is not considered) and defected surfaces as a function of wide-range temperature and oxygen pressure variations [c₁–(100) and c₂–(110)], along with the magnified fragment corresponding to the soot combustion conditions with the superimposed oxygen pressure changes observed during the TC and LC soot oxidation experiments (d).

are C¹⁶O¹⁸O and C¹⁶O₂. The observed disparity between C¹⁶O₂ and C¹⁸O₂ is striking, taking into account that an equimolar isotopic blend was used for the soot combustion in this experiment. A small content of the ¹⁶O¹⁸O isotopomer in the gas exit observed before the combustion maximum shows that all ROS produced upon dioxygen dissociation on the catalyst surface (suprafacial species) are consumed during the oxidation of soot particles. Their amount can roughly be assessed by comparison of the ¹⁶O¹⁸O profile obtained in the reference isotopic exchange in the absence of soot (see dotted line in Figure 6c₁) with that observed during the soot oxidation using the same 1:1 isotopic composition of dioxygen. Upon passing the maximum, once the soot amount ceases, the ¹⁶O¹⁸O isotopomer significantly develops, but still in a lower extent than in the reference experiment without the soot particles. The isotopic composition of CO₂, however, is substantially different than that of dioxygen. This is also revealed by the CO₂ profiles in Figure S4, simulated on the basis of a suprafacial oxidation of soot with the oxygen isotopomers produced upon the ¹⁸O₂ and ¹⁶O₂ exchange reaction on the catalyst surface shown in Figure 3b,c. This clearly reveals operation of a complex oxidation mechanism, which cannot be accounted for by a dominant contribution of the suprafacial active oxygen species only.

Such a conjecture is further supported by the results of soot combustion in ¹⁸O₂ (Figure 6d,d₁), where the disparity between the isotopic composition of carbon dioxide and dioxygen (calculated separately for each of them) is much more pronounced. As expected, the CO₂ composition is now dominated by the C¹⁸O₂ and C¹⁶O¹⁸O isotopomers, but the contribution of C¹⁶O₂ is still significant, especially in the low-temperature region. It was also found to depend on the dioxygen/soot ratio (*cf.* the combustion profile for dioxygen

partial pressure decreased by half, shown in Figure S5). Furthermore, development of C¹⁶O¹⁸O is much more intensive than that expected from the isotopic exchange of ¹⁸O₂ with the catalyst surface (see Figure 3b,c) and subsequent suprafacial soot oxidation with the resultant ¹⁶O¹⁸O (see the corresponding simulated curve in Figure S6), implying that the C¹⁶O¹⁸O species are produced in an intricate way involving the formation of oxygen vacancies as well.

3.5.2. Loose Contact Combustion. Analogous experiments performed in the LC mode show dramatic differences in the temperature progression of the soot combustion process. The reaction is not only extended toward higher temperatures (~380–710 °C), but becomes more complex, as it can be inferred from the complicated 3-modal shape of the corresponding O₂ and CO₂/CO profiles, even when the 16-labeled dioxygen only is used (Figure 7a). The onset of oxidation takes place around the temperatures observed in TC mode, but the main oxidation maximum occurs at 610 °C. A pronounced hysteresis in the normalized *p*_{O₂} vs *p*_{CO₂} plot (Figure 7b) shows that the corresponding redox changes in the K-OMS-2 catalyst state are now much more intensive and incongruent. As the reduction phase is substantially more pronounced than the oxidation one, the K-OMS-2 catalyst becomes effectively reduced at the end of the reaction. Indeed, in the XRD and RS spectra recorded upon LC soot combustion, new lines assigned to Mn₂O₃/Mn₃O₄ are easily detectable (Figure S2c1,c2), in contrast to the analogous spectra recorded upon combustion in the TC mode (Figure S2b1,b2). It should be noted that upon passing the maximum, above 630 °C, the catalyst surface recovers its redox stability, as it can be inferred from the flat ¹⁶O₂ profile and the retained

convergence of p_{O_2} and p_{CO_2} , shown in Figure 7a,b, respectively.

Combustion in a 1:1 mixture of $^{16}\text{O}_2/^{18}\text{O}_2$ (Figure 7c₁) revealed that in the whole temperature range, the dissociative oxygen activation (gauged by the $^{16}\text{O}^{18}\text{O}$ profile) is much more efficient than the soot oxidation. The combustion onset is dominated by C^{16}O_2 , but then the amount of growth of $\text{C}^{16}\text{O}^{18}\text{O}$ is significant until nearly steady isotopic composition of CO_2 and O_2 is reached. The dominant combustion maximum at 610 °C is related to the release of $^{16}\text{O}_2$ and C^{16}O_2 , accompanied by the corresponding drop in the content of other isotopomers in the exit gases (Figure 7c₁). The LC soot combustion in $^{18}\text{O}_2$ leads to a similar overall picture, and is featured by an apparently large contribution of the $^{16}\text{O}^{18}\text{O}$ and $\text{C}^{16}\text{O}^{18}\text{O}$ species in the products, with the exception of the oxidation maximum, where again $^{16}\text{O}_2$ and $^{16}\text{CO}_2$ dominate due to the already discussed surface oxygen release (Figure 3a).

Interestingly, in the temperature range 500–700 °C, variations of the isotopic profiles of O_2 and CO_2 are mutually congruent to a large extent, which may be associated with the oxidation of remote soot particles, the presence of which was revealed by TEM and XCT observations (see Figures 1 and 2). These results indicate that LC combustion of soot particles proceeds along catalytic (ignition and subsequent contiguous oxidation) and noncatalytic (burn-out) stages, which are resolved in contrast to the TC combustion, and are further discussed in more detail.

In conclusion, from the performed isotopic experiments, it turns out clearly that mechanistic analysis of the supra- and interfacial oxygen dynamics may be inconclusive, when obtained with a single-isotopic $^{16}\text{O}_2/^{18}\text{O}_2$ mixture. This is caused by the fact that several molecular events occurring simultaneously have a direct influence of the resultant isotopic composition, hindering strongly a straightforward extraction of the required information of the catalytic relevance.

3.6. DFT and Ab Initio Thermodynamic Modeling. Corroborative DFT calculations in conjunction with first principles thermodynamics were used to rationalize the cryptomelane surface redox behavior. It was found that among the low index planes compatible with the (I 4/m) structure of cryptomelane, the following (100), (110), (011), and (111) exhibit the lowest surface energies, equal to $\gamma_{100} = 0.45$, $\gamma_{110} = 0.72$, $\gamma_{011} = 0.43$, and $\gamma_{111} = 0.41$ J/m², respectively. Analysis of the shape of the K-OMS-2 nanorods observed in TEM images (Figure 1a₂) shows that the (100) and (110) terminations constituting the side planes of the nanorods have dominant contribution to the overall surface area. The optimized geometries of those terminations are shown in Figure 8a₁,a₂. Their characteristic feature is the presence of two types of surface oxygen species, namely a loosely bound O_{2c}^{2-} of the 2-fold coordination and trigonal O_{3c}^{2-} anions.

Both (100) and (110) terminations exhibit essentially the same kind of the surface O_{2c}^{2-} and O_{3c}^{2-} anions, and their particular energetic stabilities give rise to the appearance of the stoichiometric versus defected surface states under varying conditions. The considered scenarios of the oxygen vacancy formation (the type and the number of vacancies and their locations) are shown in Figure 8b₁,b₂. Thermodynamic stabilities of the corresponding surfaces as a function of T and p_{O_2} are shown in Figure 8c₁,c₂, for the (100) and (110) terminations, respectively. The dark yellow areas refer to the

stoichiometric (100) and (110) surfaces, whereas the solid lines, labeled as the corresponding vacancies shown in Figure 8b₁,b₂, delineate their defected states, containing one vacancy per 1.2 nm² for the (100) and per 1.7 nm² for the (110) plane (orange area), two vacancies (red area), and three vacancies (brown areas). However, in the case of the (110) termination, the brown area entails also the formation of a $\text{V}_{\text{O}_{3c}}$ vacancy in the 1_{3c} position, implying that in such locations, the $\text{O}_{\text{sur}}^{2-}$ anions are particularly stable. As revealed by the analysis of Figure 8d, at the oxygen pressures of the soot combustion (see the experimental p_{O_2} profiles observed during the TC and LC combustion), the stoichiometric surface is stable until ~350 °C. With the increasing temperature, the surface containing one $\text{V}_{\text{O}_{2c}}$ or $\text{V}_{\text{O}_{3c}}$ vacancy becomes the most stable state up to ~550 °C, whereas in the temperature range of 550–750 °C, the surface containing two and three oxygen $\text{V}_{\text{O}_{2c}}/\text{V}_{\text{O}_{3c}}$ vacancies dominates. Under the oxygen pressure variation during soot combustion in the LC mode, the defected surface with multiple vacancies may appear around 600 °C when the oxygen partial pressure drops below $p_{\text{O}_2}/p_0 = \sim 10^{-2}$.

The surface vacancies may diffuse toward the bulk of the cryptomelane catalyst, where they are more stable. The suprafacial ROS species produced upon interaction of dioxygen with the catalyst surface are quite softly bound, because the corresponding adsorption energies are around 1 eV, the diffusion barriers are rather small. As a result, they may participate in the soot combustion upon spillover from the catalyst surface directly onto the soot particles. Finally, it is worth mentioning that the predicted onset of oxygen vacancy formation corresponds well to the beginning of soot combustion, providing the thermodynamic rationale for the role of surface oxygen involvement in the incipient stage of the reaction.

3.7. Mechanism of Soot Oxidation. The inherent complexity of the triple phase soot-catalyst-dioxygen system with a steadily changing area of the mutual contacts with the progressing combustion, and the observed intricacy of the isotopic composition of the combustion products, with their possible subsequent scrambling, limit application of conventional kinetic modeling of the observed isotopic profiles in a tractable quantitative way. In an attempt to gain insights into the tradeoff between the suprafacial ($\text{O}_{n\text{-ads}}^-$) and intrafacial ($\text{O}_{\text{surf}}^{2-}$) oxygen involvement in the soot combustion, we have performed the experiments using variable isotopic mixtures containing 98, 50, 30, 13, and 0 mol % of $^{18}\text{O}_2$ (the further TPSR profiles for 13 and 30% are shown in Figure S7). Additionally, to simplify the analysis of the results, we use the α_{16} parameter for carbon dioxide and dioxygen to describe the isotopic effects of the oxidation process in a concise way. In a simple approach, soot oxidation may be treated in terms of concurrent involvement of the suprafacial and intrafacial oxygen species, with their relative contributions gauged by the θ and $(1 - \theta)$ parameters, respectively (see Figure 9).

The $(1 - \theta)$ parameter represents the fraction of the surface oxygen anions that participate in soot particle oxidation under given conditions, which are located in the interface between the soot particles and the catalyst surface being in an intimate contact (this region is marked by the black arrow in Figure 9), whereas θ represents the fraction of the mobile suprafacial oxygen species, which are not in direct contact with the soot particles, but may be transported diffusively into the vicinity of the triple junction before back-recombination and desorption

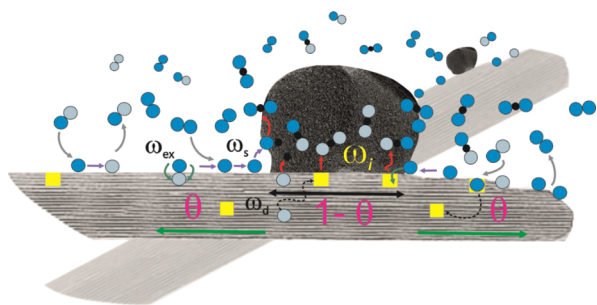


Figure 9. Schematic picture of the possible events involved in soot particle oxidation on the surface of the K-OMS-2 nanorods. The yellow squares stand for oxygen vacancies, whereas the pale blue and blue circles for the O-16 and O-18 oxygen atoms, respectively, and the black circles for carbon atoms. The green arrow indicates the region associated with the fraction, θ , of the adsorbed ROS species that may diffuse into the triple junction without prior recombination, whereas the black arrow indicates the area associated with the fraction $(1 - \theta)$ of the surface oxygen that participate in the soot oxidation.

(from the area marked by green arrows in Figure 9). Within this model, the combustion process may be treated in terms of soot particles placed on reactive bottom (catalyst surface) surrounded by the mobile ROS species (including gas-phase dioxygen reacting directly with soot particles in the late afterburning phase). Such a model resembles that proposed by Vernoux et al. for soot oxidation over yttria-stabilized zirconia.⁵⁵ ω_i and ω_s describe the individual probabilities (rates) of carbon oxidation by the intrafacial and suprafacial oxygen species, respectively, whereas ω_d and ω_{ex} stand for the probabilities of oxygen diffusion into the bulk and for the surface isotopic exchange. In such a case, the rate of soot oxidation by oxygen-18 species may be approximated as

$$r_{18} \approx \omega_s \cdot \theta \cdot (1 - q)(1 - \delta)$$

where q indicates the isotopic content of O-16 in the gas mixture (initial α_{16} value) and δ the aggregated fraction of the intrafacial O-18 loss due to exchange with the catalyst surface

(ω_{ex}) and/or diffusion into the bulk (ω_d) events. Neglecting the small mixed term $\theta \delta(1 - q)\omega_s$ (see Figures 6d₁ and S5 with the corresponding explanation in Supporting Information), the contribution of which is diminished with the increasing O-16 content in the reaction mixture ($\theta \delta(1 - q)\omega_s \rightarrow \theta \delta \omega_s$ for $q \rightarrow 0$ and to 0 for $q \rightarrow 1$), we may approximate the r_{18} rate as $r_{18} \approx \omega_s \cdot \theta \cdot (1 - a)$.

An analogous equation may be formulated for the rate of the soot oxidation by suprafacial and intrafacial oxygen-16 species.

$$r_{16} \approx \omega_s \cdot \theta \cdot q + (1 - \theta)\omega_i$$

Because the $\alpha_{16}(\text{CO}_2)$ value is defined as $r_{16}/(r_{16} + r_{18})$, then

$$\alpha_{16}(\text{CO}_2) \approx \theta[\omega_s \cdot \theta \cdot q + (1 - \theta)\omega_i] / [(\omega_s \cdot \theta \cdot q + (1 - \theta)\omega_i) + \omega_s \cdot \theta \cdot (1 - q)]$$

Taking into account quite similar energies of the lattice $\text{O}_{2c}/\text{O}_{3c}$ (0.8–1.2 eV) and surface O_{ads} (1–1.2 eV) release, we may assume that $\omega_i \approx \omega_s$. Then, upon rearrangement of the above equation, we obtain a simple linear relationship

$$\alpha_{16}(\text{CO}_2) \approx (1 - \theta) + \theta \cdot q$$

Thus, by measuring the α_{16} variation as a function of the isotopic composition q (mole % of $^{16}\text{O}_2$ in the reaction mixture) under the isothermal conditions, the relative contributions of the intra- and suprafacial mechanisms in the soot combustion can be reasonably well disentangled. The straight lines obtained while plotting $\alpha_{16}(\text{CO}_2)$ versus q shown in Figure 10a₁ confirm the overall validity of the proposed approximate model, for both the TC and LC soot oxidation. Although the isotopic composition of the suprafacial oxygen species that are in an equilibrium with the gas-phase oxygen changes linearly with q , the intrafacial fraction of the oxygen species participating in soot oxidation does not depend directly on q (at least in the first approximation). The small deviations observed at low q values (highest O-18 content) in the LC, in particular, reflect a small involvement of the isotopic surface exchange between the suprafacial O-18 and intrafacial O-16

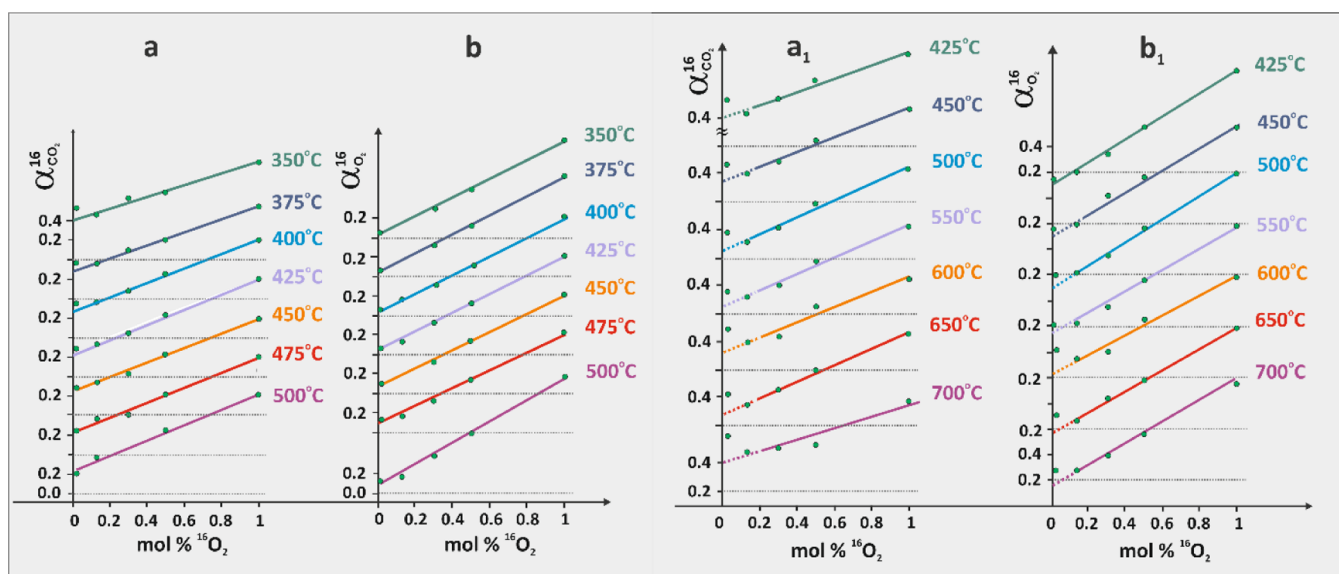


Figure 10. Variation of $\alpha_{16}(\text{CO}_2)$ (a,a₁) and $\alpha_{16}(\text{O}_2)$ (b,b₁) parameters as a function of isotopic composition of the reaction mixture, q , at various temperatures for tight (a,b) and loose (a₁,b₁) contacts, respectively. The dotted line indicates the extrapolated fragments due to deviations from the linearity caused by the enhanced isotopic exchange with the catalyst surface.

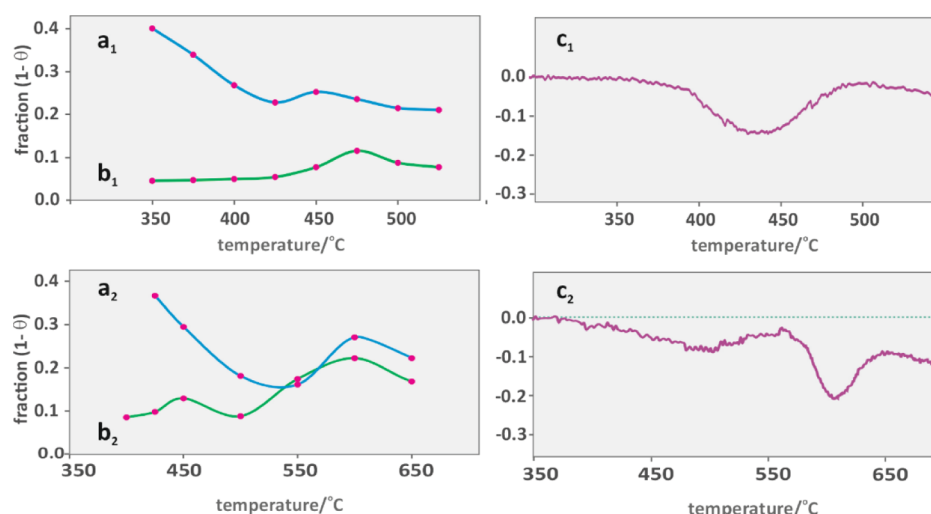


Figure 11. Temperature dependence of the CO₂ fraction produced via intrafacial oxidation directly by the lattice oxygen as a function of temperature (a₁, a₂), and the fraction of oxygen exchange with the surface (b₁, b₂). Oxygen O-18 total mass balance for soot combustion in the tight (c₁) and loose (c₂) mode.

oxygen species and/or diffusion into the catalyst bulk. However, at low temperatures, in the initial stage of combustion, the appearance of excessive O-16 labeled CO₂ species may also arise from soot decarboxylation/decarbonylation observed in the separate experiment (see Figure S3). Soot combustion with ¹⁶O₂ over the catalyst prelabeled with O-18 (Figure S8) allows for direct tracking of the transfer efficiency of ¹⁸O²⁻ species from the catalyst bulk to the surface (and then to gas-phase CO₂ and O₂ molecules) with temperature. As expected, it is small for TC combustion, gaining importance in the LC mode.

Analogous treatment of the isotopic data can be performed for dioxygen isotopomers, and indeed the corresponding α₁₆(O₂) versus *q* plots exhibit, again, a fairly good linear character as well (Figure 10b, b₁). Some deviations, particularly pronounced at higher temperatures in the case of LC combustion when the highest enrichment in ¹⁸O₂ was used (small contributions of O-16 are not buffered by the gas phase ¹⁶O₂ in such cases), are caused by surface exchange/bulk diffusion of the suprafacial O-18 species. This is indirectly confirmed by a nearly constant O_{surface}/O_{lattice} ratio (0.21–0.24:0.79–0.76), determined from the O1s XPS signal of the K-OMS-2 catalyst recorded before and after soot oxidation in the TC and LC modes (Figure S9). In order to maintain the O_{surface}/O_{lattice} ratio practically unchanged, the oxygen vacancies must efficiently diffuse to the bulk.

The slopes of the lines reflect the fraction of the suprafacial isotopic exchange due to the surface-catalyzed reaction between the dissociated ¹⁸O₂ and ¹⁶O₂ occurring in the course of soot oxidation (which is analogous to that observed in a corroborative experiment on the bare catalyst surface, shown in Figure 3d). The intercepts reveal the fraction of oxygen species exchanged with the surface during the reaction, ω_{ex} (which is analogous to that shown in Figure 3c).

As a result, discrimination between the supra- and intrafacial events involving oxygen reactive species can be assessed by tracing the evolution of the isotopic label (α₁₆) as a function of *q* at the selected constant temperature.

Variation of the (1 – θ) values with the temperature for CO₂ and O₂ are shown in Figure 11 for TC and LC combustion. Inspection of this figure shows that the soot

combustion reaction occurs along the pathways involving both the suprafacial and intrafacial oxygen species. As discussed, the results of the ab initio thermodynamic modeling suggest that, apart ROS (adsorbed O⁻/O₂⁻), the surface oxygen anions (O_{2c}²⁻ and O_{3c}²⁻) play the role of the actual oxidants. In the suprafacial pathway, soot oxidation entails spillover of the mobile ROS across the surface toward the catalyst/soot junctions, whereas in the intrafacial pathway, highly active surface O_{2c}²⁻ and O_{3c}²⁻ species that are in direct contact with the soot grains upon CO₂/CO formation leave oxygen vacancies. The latter may be partly annihilated by diffusion of the bulk O²⁻ toward the surface or refilled by adooxygen. Such a vacancy-healing process is driven by a difference in the thermodynamic stabilities between the surface (0.8–1.2 eV) and bulk (3.1 eV) oxygen vacancies. Because the isothermal VIC results of the soot oxidation were extracted from the corresponding TPSR profiles at the selected intermittent temperatures, the average number of soot–catalyst contacts in the given temperature is nearly constant. This is justified taking into account a rather small extent of the reaction progress (transient <X> is around 0.5%/°C) for the applied heating rate of 10 °C/min. Thus, the successive straight lines in Figure 10 correspond to a situation, where at a given temperature the isotopic composition varies with virtually constant θ.

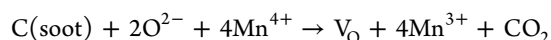
As the temperature increases, the number of direct contacts gradually decreases due to soot burn-off, so the intrafacial fraction (1 – θ) steadily decreases. The parallel profile illustrating the changes in surface oxygen dynamics (Figure 11b₁) shows that the extent of the oxygen isotopic exchange with the catalyst surface is relatively small (below 10%), as expected. It is enhanced appreciably at a temperature of the combustion maximum (~450 °C), which may be traced back to the associated local overheating effect due to abrupt combustion heat release. However, it should be emphasized that the shape of this curve, although being flattened by the concurrent soot combustion, resembles in its overall character the oxygen exchange profile observed in the absence of soot (cf. the corresponding α peak in Figure 3c, in particular), supporting indirectly the validity of the proposed model. Figure 11c₁ shows that in this temperature region, an appreciable deviation of the O-18 balance also takes place.

Both effects imply that the diffusion of the O-18 labeled species into the bulk of the K-OMS-2 catalyst is rather small (<0.15%) in the case of the TC combustion, which is reflected in the quite good linearity of both $\alpha_{16}(\text{CO}_2)$ and $\alpha_{16}(\text{O}_2)$ versus T plots (Figure 10a,b).

Analysis of the analogous profiles obtained for soot combustion in the LC (Figure 11a₂,b₂,c₂) shows a clearly different behavior of the investigated system. The intrafacial fraction of the CO_2 varies with the temperature more dramatically, and upon initial fall, it increases to a substantial extent, forming two maxima around 450 and 600 °C that coincide with the maxima in the soot combustion. The $\alpha_{16}(\text{O}_2)$ profile generally resembles the $^{18}\text{O}_2$ exchange with the bare catalyst surface Figure 3c (cf. the positions of α and β peaks, in particular), but is understandably modified by the concurrent soot combustion process. The parallel changes in the intrafacial oxygen profile (Figure 11b₂) and the O-18 balance (Figure 11c₂) as well show that the isotopic exchange with the surface and the bulk diffusion are also enhanced in this temperature region. It should be noted that the contribution of the suprafacial oxygen still dominates over the course of the whole combustion process. In contrast to the TC combustion, the observed temperature shift in the LC gives rise to an enhanced involvement of the surface oxygen. The appearance of the broad maximum at 600 °C is then caused by surface oxygen release, as revealed in the isotopic exchange experiments (Figures 3 and 7). Such loss of oxygen is reflected in the formation of $\text{Mn}_2\text{O}_3/\text{Mn}_3\text{O}_4$ phases, detected in the XRD patterns and RS spectra, recorded after the LC combustion (Figure S2), as well as by the pronounced asymmetric shape of the redox hysteresis in Figure 7b. It should be stressed, however, that the observed relative involvement of the suprafacial and intrafacial oxygen species depends essentially on the applied oxygen partial pressure, and is characteristic of the soot/catalyst/ p_{O_2} /contact type system as a whole, and not for the contact type alone. In the burn-off stage, when soot oxidation directly by dioxygen is possible, the assessed suprafacial process involves ROS and gas-phase O_2 contributions, as in the applied method both exhibit the same isotopic response.

3.8. Functional Hot Ring Model of Soot Combustion.

The obtained results can also be accounted for by the FPT modeling. Figure 8 shows that the stoichiometric K-OMS-2 surface is stable till ~350 °C. In the range of the TC combustion temperatures, the defected surface with the oxygen $\text{V}_{\text{O}_{2\text{c}}}$ and $\text{V}_{\text{O}_{3\text{c}}}$ vacancies is the most stable. This speaks in favor of direct participation of the $\text{O}_{2\text{c}}^{2-}$ and $\text{O}_{3\text{c}}^{2-}$ oxygen species in the intrafacial oxidation of soot particles (especially in the ignition stage).

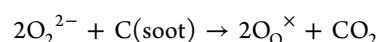
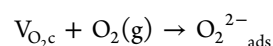


They are also intensively involved in the early and middle stages of soot oxidation in the LC mode. Above 550 °C, multiple vacancies of the $\text{V}_{\text{O}_{2\text{c}}}$ and $\text{V}_{\text{O}_{3\text{c}}}$ type are produced due to excessive oxygen release (Figure 8d), accounting for the appearance of the maximum in the LC combustion profile. The resultant highly defected K-OMS-2 surface is then partly transformed into manganese oxides of lower oxidation states. The moderately defected state of the surface is beneficial for enhancing the suprafacial pathway of soot oxidation. The resultant Mn^{3+} cations act then as the proficient centers for dioxygen activation (ROS generation)



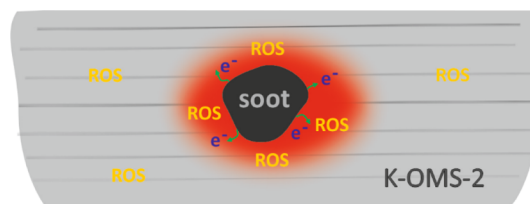
In a corroborative experiment, we found that the oxidized K-OMS-2 catalyst with the Mn/O ratio closer to the stoichiometric one (~0.5) is less active in soot combustion than the defected cryptomelane with Mn/O ~ 0.63 (Figure S10). A similar effect has also been observed in the case of benzene oxidation over cryptomelane catalysts with a various number of oxygen vacancies.⁵⁶

This confirms an important role of the manganese redox state in the efficient generation of the ROS species, implying an electronic coupling between the intrafacial and the suprafacial pathways. Alternatively, dioxygen may be activated on the vacancies (such as $\text{V}_{\text{O}_{2\text{c}}}$ or $\text{V}_{\text{O}_{3\text{c}}}$) directly producing peroxo species ($\Delta E = -1.27$ eV), acting as a source of active oxygen



Such a reaction is particularly favored in the soot particle–catalyst surface peripheries, where the vacancies are more extensively generated. As a result, the soot combustion can be rationalized in terms of a functional “hot ring” model, where a soot particle placed on the reactive bottom of cryptomelane is surrounded by a diffused collar of mobile suprafacial ROS species. As implied by the dominance of the O-16-labeled carbon dioxide species in the products, the combustion reaction is initiated by the highly active $\text{O}_{2\text{c}}^{2-}/\text{O}_{3\text{c}}^{2-}$ (100)/ $\text{O}_{2\text{c}}^{2-}$ (110) at the soot particle/catalyst interface. This leads to enhanced generation of the reduced Mn^{3+} (or even Mn^{2+}) in the vicinity of the oxidized soot particle, forming a “hot ring” of enhanced ROS production, shown in Scheme 1.

Scheme 1. Hot Ring Model of Soot Combustion



The size of this ring is determined by the extent of the electron spillover, which controls the manganese reduction, and the average range of surface diffusion of the mobile ROS during their accommodation time on surface prior the desorption. It should be mentioned here that the electrons may possibly be also transported into the triple junction via the conducting soot particles as proposed previously by Vernoux et al.⁵⁵ Within the hot ring formed around the soot particles, dioxygen activation is significantly enhanced due to extensive Mn reduction. The latter process is actually triggered by the oxidation of soot particles via the intrafacial channel that generates the requisite electrons, making the intra- and suprafacial pathways at least electronically partly coupled.

The proposed model of soot combustion is indirectly supported by the comparison of the isotopic composition of the gases observed during the $\text{C}^{16}\text{O}_2/^{18}\text{O}_2$ scrambling experiment (Figure S3c) with the corresponding isotopic composition of the products in the TC (Figure 6d₁) and LC (Figure 7d₁) soot combustion in $^{18}\text{O}_2$. The $^{16}\text{O}_2$ profiles in both soot combustion experiments are nearly stable (with the

exception of the characteristic peak at 600 °C due to oxygen release), whereas in the course of $C^{16}O_2/^{18}O_2$ scrambling, the $^{16}O_2$ content (being the product of this reaction) steadily increases until an equilibrium is reached. The $^{16}O_2$ line is thus the most diagnostic feature for detection of the scrambling. Furthermore, around 600 °C, the amount of the evolving $C^{16}O^{18}O$ and $^{16}O^{18}O$ isotopomers distinctly increases, whereas during the scrambling remains nearly constant. These findings remain in line with the proposed conjecture that ROS species, which are extensively formed in the “hot ring” area, immediately spillover onto the soot grain to produce CO_2 . As a result, the scrambling is greatly attenuated in comparison to the reaction performed on the bare K-OMS-2 catalyst, where this process extends over the whole surface.

Summarizing, the TC combustion proceeds mainly with involvement of the ROS adspecies, and is accomplished with the single exotherm. The redox hysteresis is small, and the catalyst resumes its redox state readily. Owing to the compact packing, the generated heat is conserved, facilitating the afterburning in the late stages of the reaction. Because the O_{sur}^{2-} oxygen species initiate the reaction (see the isotopic composition variations in Figure 6), the abundant soot particle/surface contacts are particularly beneficial. As a result, the catalyst acts as an igniter in the beginning, and as a ROS generator during the mature phase of the combustion.

In the LC mode, the large voids and a small number of the mutual contacts attenuate the abrupt ignition (Figures 1 and 2), therefore, the combustion is extended with temperature, proceeding in a multimodal way. Paradoxically, the catalyst is more intensively engaged during this process, the redox hysteresis is large, and due to the prolonged net oxygen release, the catalyst surface becomes finally reduced. In the combustion process, the gas-phase oxygen more strongly interacts with the surface, and the redox coupling (oxygen vacancy exchange) between the surface and the bulk also gains importance. The local heat generated in the course of the reaction being lost to a substantial extent is now not ample enough to support the autogenous afterburning efficiently. Thus, the catalyst acts mostly as a booster that drives the combustion process for the dominant part of its entire duration.

The described mechanistic studies of the K-OMS-2 catalyst were performed under model conditions, which are favorable for revealing the complex oxygen dynamics during the soot combustion process. Investigation into the cryptomelane catalyst activity in the presence of NO_x (intentionally not examined in this work for the sake of the system simplicity) is now in progress using isotopically labeled reactants, and will be the subject of our forthcoming paper. Furthermore, although in the LC mode, the catalyst is partly reduced at the end of the catalytic cycle, in the presence of NO_x the temperature window of the LC combustion is shifted substantially toward lower temperatures (by 80 °C), where the cryptomelane catalyst is redox stable. The K-OMS-2 stability may also be improved by suitable doping with alien ions,²³ whereas the temperature window of the catalyst in the LC may be lowered substantially by dispersion of the cryptomelane nanobars on the support.⁵⁷ This supports well potential applications of the catalyst based on the cryptomelane backbone, owing to its unique redox features and straightforward availability of the surface oxygen.

4. CONCLUSIONS

The performance of a cryptomelane model catalyst in soot combustion was thoroughly investigated in the TC and LC,

using isotopic $^{18}O_2/^{16}O_2$ mixtures of various compositions. The relative involvement of the suprafacial and intrafacial reactive oxygen species in the soot oxidation was disentangled by applying the developed model of isotopic data analysis. The corroborative DFT and atomistic thermodynamic modeling allowed for the identification of the low-coordinated O_{2c} and O_{3c} oxygen anions located on the (100) and (110) planes as the essential surface-active species involved in the ignition process, which act in concert with ROS and gas-phase oxygen in the soot burning. A functional “hot ring model” was established to rationalize the nature of the catalyst operation. Apart from the ROS generation function, the catalyst acts as an igniter in the TC mode, whereas in the LC mode as a booster that drives the combustion process until the autogenous combustion stage is reached.

■ ASSOCIATED CONTENT

Supporting Information

The Supporting Information is available free of charge at <https://pubs.acs.org/doi/10.1021/acscatal.1c02152>.

μ -CT scanning setup, XRD patterns, Raman spectra, isotopic scrambling, and reference TPSR results along with simulations of CO_2 profiles (PDF)

■ AUTHOR INFORMATION

Corresponding Authors

Joanna Gryboś – Faculty of Chemistry, Jagiellonian University, Krakow 30-387, Poland; orcid.org/0000-0002-9777-0268; Phone: +48 12 686 2508; Email: sojka@chemia.uj.edu.pl; Fax: +48 12 686 2750

Zbigniew Sojka – Faculty of Chemistry, Jagiellonian University, Krakow 30-387, Poland; orcid.org/0000-0001-7226-7626; Email: grybosjo@chemia.uj.edu.pl

Authors

Monika Fedyna – Faculty of Chemistry, Jagiellonian University, Krakow 30-387, Poland

Piotr Legutko – Faculty of Chemistry, Jagiellonian University, Krakow 30-387, Poland

Bartosz Leszczyński – Faculty of Physics, Astronomy and Applied Computer Science, Jagiellonian University, Krakow 30-348, Poland

Janusz Janas – Faculty of Chemistry, Jagiellonian University, Krakow 30-387, Poland

Anna Wach – Institute of Nuclear Physics, Polish Academy of Sciences, Krakow 31-342, Poland; orcid.org/0000-0003-3112-2759

Jakub Szlachetko – Institute of Nuclear Physics, Polish Academy of Sciences, Krakow 31-342, Poland; orcid.org/0000-0002-7526-3097

Xuehua Yu – Institute of Catalysis for Energy and Environment, College of Chemistry and Chemical Engineering, Shenyang Normal University, Shenyang 110034 Liaoning, China; orcid.org/0000-0002-4609-1097

Andrzej Kotarba – Faculty of Chemistry, Jagiellonian University, Krakow 30-387, Poland; orcid.org/0000-0003-4815-0051

Zhen Zhao – Institute of Catalysis for Energy and Environment, College of Chemistry and Chemical Engineering, Shenyang Normal University, Shenyang 110034 Liaoning, China; orcid.org/0000-0003-0044-5512

Complete contact information is available at:

<https://pubs.acs.org/10.1021/acscatal.1c02152>

Funding

This work was carried out within the MOST program for bilateral collaboration between Poland and China, which is financially supported by The National Center for Research and Development, Poland, grant PNOX (WPC1/PNOX/2019) and from the China side by the Key Research and Development Program of MOST (2017YFE0131200).

Notes

The authors declare no competing financial interest.

ACKNOWLEDGMENTS

We acknowledge the Paul Scherrer Institute, Villigen, Switzerland for provision of the synchrotron radiation beamtime at beamline SuperXAS of the SLS.

REFERENCES

- (1) Van Setten, B. A. A. L.; Makkee, M.; Moulijn, J. A. Science and Technology of Catalytic Diesel Particulate Filters. *Catal. Rev.—Sci. Eng.* **2001**, *43*, 489–564.
- (2) Wei, E. T.; Shu, H. P. Nitroaromatic Carcinogens in Diesel Soot: A Review of Laboratory Findings. *Am. J. Publ. Health* **1983**, *73*, 1085–1088.
- (3) Fino, D. Diesel Emission Control: Catalytic Filters for Particulate Removal. *Sci. Technol. Adv. Mater.* **2007**, *8*, 93–100.
- (4) Johnson, T. V. Diesel Emission Control in Review. *SAE Technical Papers*, 2009, pp 1–12.
- (5) Teraoka, Y.; Shanguan, W. F.; Kagawa, S. Reaction Mechanism of Simultaneous Catalytic Removal of NO_x and Diesel Soot Particulates. *Res. Chem. Intermed.* **2000**, *26*, 201–206.
- (6) Fino, D.; Bensaid, S.; Piumetti, M.; Russo, N. A Review on the Catalytic Combustion of Soot in Diesel Particulate Filters for Automotive Applications: From Powder Catalysts to Structured Reactors. *Appl. Catal., A* **2016**, *509*, 75–96.
- (7) Hernández-Giménez, A. M.; Castelló, D.; Bueno-López, A. Diesel Soot Combustion Catalysts: Review of Active Phases. *Chem. Pap.* **2014**, *68*, 1154–1168.
- (8) Jiménez, R.; García, X.; López, T.; Gordon, A. L. Catalytic Combustion of Soot. Effects of Added Alkali Metals on CaO-MgO Physical Mixtures. *Fuel Process. Technol.* **2008**, *89*, 1160–1168.
- (9) Jakubek, T.; Kaspera, W.; Legutko, P.; Stelmachowski, P.; Kotarba, A. How to Efficiently Promote Transition Metal Oxides by Alkali Towards Catalytic Soot Oxidation. *Top. Catal.* **2016**, *59*, 1083–1089.
- (10) Thrimurthulu, G.; Rao, K. N.; Devaiah, D.; Reddy, B. M. Nanocrystalline Ceria-Praseodymia and Ceria-Zirconia Solid Solutions for Soot Oxidation. *Res. Chem. Intermed.* **2012**, *38*, 1847–1855.
- (11) Aneggi, E.; de Leitenburg, C.; Dolcetti, G.; Trovarelli, A. Diesel Soot Combustion Activity of Ceria Promoted with Alkali Metals. *Catal. Today* **2008**, *136*, 3–10.
- (12) Xie, Y.; Zhang, C.; Wang, D.; Lu, J.; Wang, Y.; Wang, J.; Zhang, L.; Zhang, R. Catalytic Performance of a Bi₂O₃-Fe₂O₃ System in Soot Combustion. *New J. Chem.* **2019**, *43*, 15368–15374.
- (13) Mori, K.; Iwata, Y.; Yamamoto, M.; Kimura, N.; Miyauchi, A.; Okamoto, G.; Toyoshima, T.; Yamashita, H. An Efficient Cu/BaO/La₂O₃ Catalyst for the Simultaneous Removal of Carbon Soot and Nitrogen Oxides from Simulated Diesel Exhaust. *J. Phys. Chem. C* **2014**, *118*, 9078–9085.
- (14) Yu, X.; Wang, L.; Zhao, Z.; Fan, X.; Chen, M.; Wei, Y.; Liu, J. 3DOM SiO₂-Supported Different Alkali Metals-Modified MnO_x Catalysts: Preparation and Catalytic Performance for Soot Combustion. *ChemistrySelect* **2017**, *2*, 10176–10185.
- (15) Yu, X.; Zhao, Z.; Wei, Y.; Liu, J.; Li, J.; Duan, A.; Jiang, G. Three-Dimensionally Ordered Macroporous SiO₂-Supported Transition Metal Oxide Catalysts: Facile Synthesis and High Catalytic Activity for Diesel Soot Combustion. *RSC Adv.* **2015**, *5*, 49780–49790.
- (16) Kuwahara, Y.; Kato, G.; Fujibayashi, A.; Mori, K.; Yamashita, H. Diesel Soot Combustion over Mn₂O₃ Catalysts with Different Morphologies: Elucidating the Role of Active Oxygen Species in Soot Combustion. *Chem. Asian J.* **2020**, *15*, 2005–2014.
- (17) Atribak, I.; Bueno-López, A.; García-García, A.; Navarro, P.; Frías, D.; Montes, M. Catalytic Activity for Soot Combustion of Birnessite and Cryptomelane. *Appl. Catal., B* **2010**, *93*, 267–273.
- (18) Chen, X.; Shen, Y.-F.; Suib, S. L.; O'Young, C. L. Characterization of Manganese Oxide Octahedral Molecular Sieve (M-OMS-2) Materials with Different Metal Cation Dopants. *Chem. Mater.* **2002**, *14*, 940–948.
- (19) Wasalathanthri, N. D.; SantaMaria, T. M.; Kriz, D. A.; Dissanayake, S. L.; Kuo, C.-H.; Biswas, S.; Suib, S. L. Mesoporous Manganese Oxides for NO₂ Assisted Catalytic Soot Oxidation. *Appl. Catal., B* **2017**, *201*, 543–551.
- (20) Kaspera, W.; Indyka, P.; Sojka, Z.; Kotarba, A. Bridging the Gap between Tight and Loose Contacts for Soot Oxidation by Vanadium Doping of Cryptomelane Nanorods Catalyst Using NO₂ as an Oxygen Carrier. *Catal. Sci. Technol.* **2018**, *8*, 3183–3192.
- (21) Wasalathanthri, N. D.; Guild, C.; Nizami, Q. A.; Dissanayake, S. L.; He, J.; Kerns, P.; Fee, J.; Achola, L.; Rathnayake, D.; Weerakkody, C.; Suib, S. L.; Nandi, P. Niobium-Substituted Octahedral Molecular Sieve (OMS-2) Materials in Selective Oxidation of Methanol to Dimethoxymethane. *RSC Adv.* **2019**, *9*, 32665–32673.
- (22) Sultana, S.; Ye, Z.; Veerapandian, S. K. P.; Löfberg, A.; De Geyter, N.; Morent, R.; Giraudon, J.-M.; Lamonier, J.-F. Synthesis and Catalytic Performances of K-OMS-2, Fe/K-OMS-2 and Fe-K-OMS-2 in Post Plasma-Catalysis for Dilute TCE Abatement. *Catal. Today* **2018**, *307*, 20–28.
- (23) Ma, J.; Wang, C.; He, H. Transition Metal Doped Cryptomelane-Type Manganese Oxide Catalysts for Ozone Decomposition. *Appl. Catal., B* **2017**, *201*, 503–510.
- (24) Jakubek, T.; Hudy, C.; Indyka, P.; Nowicka, E.; Golunski, S.; Kotarba, A. Effect of Noble Metal Addition to Alkali-Exchanged Cryptomelane on the Simultaneous Soot and VOC Combustion Activity. *Catal. Commun.* **2019**, *132*, 105807.
- (25) Bueno-López, A. Diesel Soot Combustion Ceria Catalysts. *Appl. Catal., B* **2014**, *146*, 1–11.
- (26) Castoldi, L. An Overview on the Catalytic Materials Proposed for the Simultaneous Removal of NO_x and Soot. *Materials* **2020**, *13*, 3551.
- (27) Stanmore, B. R.; Brillhac, J. F.; Gilot, P. The Oxidation of Soot: A Review of Experiments, Mechanisms and Models. *Carbon N. Y.* **2001**, *39*, 2247–2268.
- (28) Aneggi, E.; De Leitenburg, C.; Trovarelli, A. On the Role of Lattice/Surface Oxygen in Ceria-Zirconia Catalysts for Diesel Soot Combustion. *Catal. Today* **2012**, *181*, 108–115.
- (29) Shang, Z.; Sun, M.; Chang, S.; Che, X.; Cao, X.; Wang, L.; Guo, Y.; Zhan, W.; Guo, Y.; Lu, G. Activity and Stability of Co₃O₄-Based Catalysts for Soot Oxidation: The Enhanced Effect of Bi₂O₃ on Activation and Transfer of Oxygen. *Appl. Catal., B* **2017**, *209*, 33–44.
- (30) Wagloehner, S.; Nitzner-Noski, M.; Kureti, S. Oxidation of Soot on Manganese Oxide Catalysts. *Chem. Eng. J.* **2015**, *259*, 492–504.
- (31) Mars, P.; van Krevelen, D. W. Oxidations Carried out by Means of Vanadium Oxide Catalysts. *Chem. Eng. Sci.* **1954**, *3*, 41–59.
- (32) Fino, D.; Russo, N.; Saracco, G.; Specchia, V. The Role of Suprafacial Oxygen in Some Perovskites for the Catalytic Combustion of Soot. *J. Catal.* **2003**, *217*, 367–375.
- (33) Wang, X.; Zhang, Y.; Li, Q.; Wang, Z.; Zhang, Z. Identification of Active Oxygen Species for Soot Combustion on LaMnO₃ Perovskite. *Catal. Sci. Technol.* **2012**, *2*, 1822–1824.
- (34) Liu, S.; Wu, X.; Liu, W.; Chen, W.; Ran, R.; Li, M.; Weng, D. Soot Oxidation over CeO₂ and Ag/CeO₂: Factors Determining the Catalyst Activity and Stability during Reaction. *J. Catal.* **2016**, *337*, 188–198.

- (35) Harada, K.; Oishi, T.; Hamamoto, S.; Ishihara, T. Lattice Oxygen Activity in Pr- and La-Doped CeO₂ for Low-Temperature Soot Oxidation. *J. Phys. Chem. C* **2014**, *118*, 559–568.
- (36) Haneda, M.; Taguchi, R.; Hattori, M. Influence of Particle Morphology on Catalytic Performance of CeO₂/ZrO₂ for Soot Oxidation. *J. Ceram. Soc. Jpn.* **2015**, *123*, 414–418.
- (37) Martínez-Munuera, J. C.; Zoccoli, M.; Giménez-Mañogil, J.; García-García, A. Lattice Oxygen Activity in Ceria-Praseodymia Mixed Oxides for Soot Oxidation in Catalysed Gasoline Particle Filters. *Appl. Catal., B* **2019**, *245*, 706–720.
- (38) Obeid, E.; Tsampas, M. N.; Jonet, S.; Boréave, A.; Burel, L.; Steil, M. C.; Blanchard, G.; Pajot, K.; Vernoux, P. Isothermal Catalytic Oxidation of Diesel Soot on Yttria-Stabilized Zirconia. *Solid State Ionics* **2014**, *262*, 253–256.
- (39) Serve, A.; Boreave, A.; Cartoixa, B.; Pajot, K.; Vernoux, P. Synergy between Ag Nanoparticles and Yttria-Stabilized Zirconia for Soot Oxidation. *Appl. Catal., B* **2019**, *242*, 140–149.
- (40) Bueno-López, A.; Krishna, K.; van der Linden, B.; Mul, G.; Moulijn, J. A.; Makkee, M. On the Mechanism of Model Diesel Soot-O₂ Reaction Catalysed by Pt-Containing La³⁺-Doped CeO₂. A TAP Study with Isotopic O₂. *Catal. Today* **2007**, *121*, 237–245.
- (41) Müller, C. A.; Maciejewski, M.; Koeppel, R. A.; Tschan, R.; Baiker, A. Role of Lattice Oxygen in the Combustion of Methane over PdO/ZrO₂: Combined Pulse TG/DTA and MS Study with ¹⁸O-Labeled Catalyst. *J. Phys. Chem.* **1996**, *100*, 20006–20014.
- (42) Feldkamp, L. A.; Davis, L. C.; Kress, J. W. Practical Cone-Beam Algorithm. *J. Opt. Soc. Am. A* **1984**, *1*, 612.
- (43) Klier, K.; Novakova, J.; Jiru, P. Exchange reactions of oxygen between oxygen molecules and solid oxides. *J. Catal.* **1963**, *2*, 479–484.
- (44) Hafner, J. Ab-Initio Simulations of Materials Using VASP: Density-Functional Theory and Beyond. *J. Comput. Chem.* **2008**, *29*, 2044–2078.
- (45) Monkhorst, H. J.; Pack, J. D. Special Points for Brillouin-Zone Integrations. *Phys. Rev. B* **1976**, *13*, 5188–5192.
- (46) Reuter, K.; Scheffler, M. Composition, Structure, and Stability of RuO₂ (110) as a Function of Oxygen Pressure. *Phys. Rev. B: Condens. Matter Mater. Phys.* **2001**, *65*, 035406.
- (47) Raybaud, P.; Costa, D.; Valero, M. C.; Arrouvel, C.; Digne, M.; Sautet, P.; Toulhoat, H. First Principles Surface Thermodynamics of Industrial Supported Catalysts in Working Conditions. *J. Phys. Condens. Matter* **2008**, *20*, 064235.
- (48) Hirano, T. *MOPAC Manual*; (7th Edition); MOPAC Man, 1993, No. January.
- (49) Vicat, J.; Fanchon, E.; Strobel, P.; Tran Qui, D. The Structure of K_{1.33}Mn₈O₁₆ and Cation Ordering in Hollandite-Type Structures. *Acta Crystallogr. Sect. B Struct. Sci.* **1986**, *42*, 162–167.
- (50) Gao, T.; Glerup, M.; Krumeich, F.; Nesper, R.; Fjellvåg, H.; Norby, P. Microstructures and Spectroscopic Properties of Cryptomelane-Type Manganese Dioxide Nanofibers. *J. Phys. Chem. C* **2008**, *112*, 13134–13140.
- (51) Legutko, P.; Gryboś, J.; Fedyna, M.; Janas, J.; Wach, A.; Szlachetko, J.; Adamski, A.; Yu, X.; Zhao, Z.; Kotarba, A.; Sojka, Z. Soot Combustion over Niobium-Doped Cryptomelane (K-OMS-2) Nanorods—Redox State of Manganese and the Lattice Strain Control the Catalysts Performance. *Catalysts* **2020**, *10*, 1390.
- (52) Zasada, F.; Janas, J.; Piskorz, W.; Gorczyńska, M.; Sojka, Z. Total Oxidation of Lean Methane over Cobalt Spinel Nanocubes Controlled by the Self-Adjusted Redox State of the Catalyst: Experimental and Theoretical Account for Interplay between the Langmuir-Hinshelwood and Mars-Van Krevelen Mechanisms. *ACS Catal.* **2017**, *7*, 2853–2867.
- (53) Zhang, D.; Kawada, T.; Yoshioka, F.; Machida, M. Oxygen Gateway Effect of CeO₂/La₂O₂SO₄ Composite Oxygen Storage Materials. *ACS Omega* **2016**, *1*, 789–798.
- (54) Zasada, F.; Piskorz, W.; Stelmachowski, P.; Legutko, P.; Kotarba, A.; Sojka, Z. Density Functional Theory Modeling and Time-of-Flight Secondary Ion Mass Spectrometric and X-Ray Photoelectron Spectroscopic Investigations into Mechanistic Key Events of Coronene Oxidation: Toward Molecular Understanding of Soot Combustion. *J. Phys. Chem. C* **2015**, *119*, 6568–6580.
- (55) Obeid, E.; Lizarraga, L.; Tsampas, M. N.; Cordier, A.; Boréave, A.; Steil, M. C.; Blanchard, G.; Pajot, K.; Vernoux, P. Continuously Regenerating Diesel Particulate Filters Based on Ionically Conducting Ceramics. *J. Catal.* **2014**, *309*, 87–96.
- (56) Hou, J.; Li, Y.; Liu, L.; Ren, L.; Zhao, X. Effect of Giant Oxygen Vacancy Defects on the Catalytic Oxidation of OMS-2 Nanorods. *J. Mater. Chem. A* **2013**, *1*, 6736–6741.
- (57) Yu, X.; Zhao, Z.; Wei, Y.; Liu, J. Ordered Micro/Macro Porous K-OMS-2/SiO₂ Nanocatalysts: Facile Synthesis, Low Cost and High Catalytic Activity for Diesel Soot Combustion. *Sci. Rep.* **2017**, *7*, 43894.